

The Complex Space Weather Events of September 2017

Rajkumar Hajra¹, Bruce, T. Tsurutani², and Gurbax, S. Lakhina³

¹National Atmospheric Research Laboratory

²Jet Propulsion Laboratory, California Institute of Technology

³Indian Institute of Geomagnetism

November 21, 2022

Abstract

The complex magnetospheric and ionospheric events during September 2017 are studied. There were 4 X-class, 27 M-class and numerous C-class flares related to ~68 coronal mass ejections (CMEs), 4 of which were halo CMEs. Of the 4 halo CMEs, only 3 reached the Earth. A fast interplanetary-CME (ICME) created an upstream sheath that caused an intense magnetic storm (SYM-H peak = -146 nT). This was followed by another intense storm (SYM-H peak = -115 nT) caused by the magnetic cloud (MC) portion of the ICME. Two moderate storms (with SYM-H peaks of -65 nT and -74 nT) were caused by a sheath associated with another halo CME and a corotating interaction region (CIR), respectively. The solar wind high-speed streams (HSSs) led to continuous substorm and convection events but no magnetic storms. Fast forward shocks (FSs) and reverse waves (RWs) associated with the fast CMEs and CIRs, and heliospheric current sheet/heliospheric plasma sheet encounters were detected. The FSs and RWs caused positive and negative sudden impulses, respectively. Half of the FSs triggered substorm onsets and the RWs caused substorm recovery phases. While the FSs led to magnetospheric relativistic electron decreases, electron accelerations were associated with the MC and the HSSs. During main phases of the intense storms, two supersubstorms (SSSs) were detected, one triggered by a FS and the other by a non-shock ram pressure pulse. The SSSs caused major geomagnetically induced currents. CME propagation codes were tested with errors in arrival times ranging from ~24 min to > 35 h.

The Complex Space Weather Events of September 2017

Rajkumar Hajra^{1,*}, Bruce T. Tsurutani², and Gurbax S. Lakhina³

¹National Atmospheric Research Laboratory, Gadanki, India

²Jet Propulsion Laboratory, California Institute of Technology, Pasadena, California, USA

³Indian Institute of Geomagnetism, Navi Mumbai, India

*Corresponding author: Rajkumar Hajra (rajkumarhajra@yahoo.co.in)

Key Points

- Extreme space weather events can occur during a descending-to-minimum phase of a solar cycle
- Varying geomagnetic impacts of interplanetary shocks, waves, HCSs/HPSs, sheaths, MCs, CIRs and HSSs are studied and explained
- Solar sources and interplanetary characters of the space weather events are identified

Abstract

The complex magnetospheric and ionospheric events during September 2017 are studied. There were 4 X-class, 27 M-class and numerous C-class flares related to ~68 coronal mass ejections (CMEs), 4 of which were halo CMEs. Of the 4 halo CMEs, only 3 reached the Earth. A fast interplanetary-CME (ICME) created an upstream sheath that caused an intense magnetic storm (SYM-H peak = -146 nT). This was followed by another intense storm (SYM-H peak = -115 nT) caused by the magnetic cloud (MC) portion of the ICME. Two moderate storms (with SYM-H peaks of -65 nT and -74 nT) were caused by a sheath associated with another halo CME and a corotating interaction region (CIR), respectively. The solar wind high-speed streams (HSSs) led to continuous substorm and convection events but no magnetic storms. Fast forward shocks (FSs) and reverse waves (RWs) associated with the fast CMEs and CIRs, and heliospheric current sheet/heliospheric plasma sheet encounters were detected. The FSs and RWs caused positive and negative sudden impulses, respectively. Half of the FSs triggered substorm onsets and the RWs caused substorm recovery phases. While the FSs led to magnetospheric relativistic electron decreases, electron accelerations were associated with the MC and the HSSs. During main phases of the intense storms, two supersubstorms (SSSs) were detected, one triggered by a FS and the other by a non-shock ram pressure pulse. The SSSs caused major geomagnetically induced currents. CME propagation codes were tested with errors in arrival times ranging from ~24 min to > 35 h.

Keywords

Solar flare; CME/ICME; CIR; Interplanetary shock; HCS/HPS; Substorm

51 1. Introduction

52

53 The goal of this work is to comprehensively explore the geoeffectiveness of the space weather
54 events during the entire month of September 2017, an extremely active solar interval. Although
55 this interval was in a descending-to-minimum phase of a solar cycle (SC), this was
56 characterized by multiple solar and interplanetary events, such as 4 X-class, 27 M-class and
57 numerous C-class solar flares, and ~68 coronal mass ejections (CMEs) including 4 halo events.
58 There were 3 coronal holes (CHs) emitting high-speed (defined as $V_{sw} > 550 \text{ km s}^{-1}$) streams
59 (HSSs) during the interval. This multitude of solar activity filled interplanetary space between
60 the Sun and 1 AU.

61

62 While some aspects of the extreme flares during this interval and their effects have been
63 reported in the literature (e.g., Chamberlin et al., 2018; Chertok et al., 2018; Schillings et al.,
64 2018; Shen et al., 2018; Yan et al., 2018; Zou et al., 2019), there is no complete study on the
65 complex space weather events during this entire month. This solar activity and the
66 consequential space weather effects are particularly interesting because of the phase of the solar
67 cycle that they occurred in. As an example, Tsurutani et al. (1992), Echer et al. (2008) and
68 Meng et al. (2019) have noted the occurrence of superstorms (with Dst/SYM-H peak ≤ -250
69 nT) during solar minimum and the solar ascending phase. Although no superstorm occurred
70 during this interval of study, the solar and interplanetary complexity of this interval makes it a
71 compelling study which will lead to better understanding of space weather overall.

72

73 Fast interplanetary CMEs (ICMEs) generate antisunward shocks and sheaths of compressed,
74 heated and turbulent solar wind plasma and large amplitude magnetic field variations (e.g.,
75 Kennel et al., 1985; Tsurutani et al., 1988). Shocks can trigger substorms (Akasofu & Chao,
76 1980; Zhou & Tsurutani, 2001; Meurant et al., 2005; Hajra & Tsurutani, 2018a). Extremely
77 intense substorms or supersubstorms (SSSs: Tsurutani et al., 2015; Hajra et al., 2016; Hajra &
78 Tsurutani, 2018a) have been speculated to cause geomagnetically induced currents (GICs) at
79 the Earth. If the interplanetary sheaths contain southward interplanetary magnetic field (IMF)
80 components, they can create magnetic storms (Tsurutani et al., 1988; Zhang et al., 2007; Echer
81 et al., 2008; Meng et al., 2019) through the process of magnetic reconnection (Dungey, 1961).
82 It is also well-known that the magnetic cloud (MC: Burlaga et al., 1981; Klein & Burlaga,
83 1982) portions of ICMEs can also create magnetic storms if they contain southward IMFs
84 (Gonzalez et al., 1994). HSSs interacting with upstream slow-speed ($\sim 350\text{-}400 \text{ km s}^{-1}$) streams
85 lead to the creation of interplanetary compressed regions called corotating interaction regions
86 (CIRs: Smith & Wolfe, 1976; Pizzo, 1985; Balogh et al., 1999). CIRs can cause magnetic
87 storms which are generally weak in intensity because of the highly fluctuating IMF B_z therein
88 (Tsurutani et al., 1995). However, their trailing HSS proper can create high-intensity long-
89 duration continuous AE activity (HILDCAA: Tsurutani & Gonzalez, 1987; Tsurutani et al.
90 2006). HILDCAAs have been reported to be associated with the acceleration of
91 magnetospheric relativistic electrons (e.g., Hajra et al., 2014) in the outer zone radiation belt
92 (Van Allen & Frank, 1959). The losses of these relativistic magnetospheric electrons has also
93 been ascribed to both interplanetary (e.g., Tsurutani et al., 2016) and magnetospheric causes
94 (Baker et al., 1994; Horne et al., 2009; Hudson et al., 2014; Hajra & Tsurutani, 2018b). These
95 latter two topics will also be explored in this paper.

96

97 Several empirical models (e.g., Gopalswamy et al., 2001; Michalek et al., 2004) are available
98 in literature to predict the propagation of CMEs from the Sun to Earth. The predicted time
99 delays and the accuracy of being able to identify the flares/CMEs responsible for the
100 shocks/ICMEs at Earth will be tested by applying these codes to the available data.

101
 102 We will study space weather features, from the Sun to the Earth's ionosphere for the month of
 103 September 2017. In attempting to do this we will first have to identify the main plasma and
 104 magnetic field features in the solar wind and then relate them to the features in the
 105 magnetosphere and ionosphere to determine if they are geoeffective or not. In doing so we will
 106 be following a technique that was used by Tsurutani et al. (1988), Gonzalez et al. (1989) and
 107 Tang et al. (1989) where one first studies geomagnetic activity at the Earth and then work
 108 backwards to interplanetary space and then to the Sun. We will also test propagation codes
 109 which relate the solar flares/CMEs to ICMEs detected at 1 AU as mentioned above.

111 **2. Data and Method of Analyses**

113 *Solar Flares, CMEs and CHs*

114
 115 Space weather events occurring during September 2017 are explored in this work. To detect
 116 the solar flares, we use the X-ray fluences measured by the Solar X-ray Imager (SXI) onboard
 117 the Geostationary Operational Environmental Satellite 15 (GOES 15: Onsager et al., 1996).
 118 These data can be found at: <https://www.goes.noaa.gov/>. The CMEs are observed by the Large
 119 Angle and Spectrometric Coronagraph (LASCO) onboard the Solar and Heliospheric
 120 Observatory (SOHO: Domingo et al., 1995) (<https://sohowww.nascom.nasa.gov/>). The solar
 121 coronal images taken by the Atmospheric Imaging Assembly (AIA: Lemen et al., 2012)
 122 telescope onboard the NASA Solar Dynamics Observatory (SDO) are utilized to identify CHs
 123 (<https://sdo.gsfc.nasa.gov/>).

124
 125 We will estimate the probable propagation times of the halo CMEs to ~1 AU using empirical
 126 CME arrival model developed by Gopalswamy et al. (2001). In this model the CME is assumed
 127 to accelerate from the Sun up to ~0.76 AU, after which it is assumed to travel at a constant
 128 speed thereafter. Based on a few CME observations, the CME acceleration was expressed as:
 129 $a = 2.193 - 0.0054V_{\text{CME}}$, where a is the acceleration and V_{CME} is CME speed near the Sun.
 130 Based on observations during 49 CME events, Michalek et al. (2004) developed an "improved"
 131 expression for this acceleration as: $a = 4.11 - 0.0063V_{\text{CME}}$. By excluding the extremely slow
 132 and fast events from their database, a third expression was developed: $a = 3.35 - 0.0074V_{\text{CME}}$.
 133 In this present work, we will test above three acceleration expressions and estimate the probable
 134 CME arrival times to determine whether we can now predict the arrival times of ICMEs at
 135 Earth during extremely active solar intervals. These three propagation models are hereafter
 136 referred to as Mod1, Mod2 and Mod3, respectively. The CME list and near-Sun CME
 137 parameters are collected from the SOHO/LASCO CME catalogue
 138 (https://cdaw.gsfc.nasa.gov/CME_list/index.html).

140 *Interplanetary discontinuities*

141
 142 To study the interplanetary characteristics of the space weather events, the solar wind plasma
 143 and IMFs are obtained from the NASA WIND spacecraft (<https://wind.gsfc.nasa.gov/>)
 144 stationed in a halo orbit around the L1 Lagrange point, ~238 Earth radii upstream of the Earth.
 145 The IMFs will be displayed in geocentric solar magnetospheric (GSM) coordinates, where the
 146 x-axis is directed towards the Sun, the y-axis is in the $\Omega \times \hat{x}/|\Omega \times \hat{x}|$ direction where Ω is
 147 aligned with the magnetic south pole axis. The z-axis completes a right-hand system.

148
 149 To identify the nature of an interplanetary discontinuity, we estimated the normal (θ_{Bn}) to the
 150 discontinuity relative to the upstream IMF using the Abraham-Shrauner (1972) mixed-mode

151 method. To determine if the discontinuity is a fast shock or instead a submagnetosonic wave,
 152 the Rankine-Hugoniot conservation equations are applied to high-time resolution (~3 sec)
 153 upstream and downstream plasmas (Smith, 1985; Tsurutani & Lin, 1985; Tsurutani et al.,
 154 2011). The magnetosonic Mach number (MMN) is estimated by comparing the discontinuity
 155 speed to the calculated upstream magnetosonic wave speed.

156

157 Apart from the shocks and waves, there is another major and sometimes important
 158 discontinuity detected in the interplanetary data. This is called heliospheric current sheet
 159 (HCS). HCSs can be identified by simultaneous polarity reversals of the IMF B_x and B_y
 160 components (Ness & Wilcox, 1964; Smith et al., 1978; Tsurutani et al., 1995). A high plasma
 161 density region adjacent to the HCS has been named the heliospheric plasma sheet (HPS:
 162 Winterhalter et al., 1994). Both HCSs and HPSs are found to play space weather roles in this
 163 active interval of study.

164

165 *ICMEs, HSSs and CIRs*

166

167 CMEs propagating through interplanetary space are known as ICMEs. This is because not all
 168 3 parts of a CME, namely MC, coronal loop and a filament (Illing & Hundhausen, 1986), are
 169 detected at 1 AU. Furthermore, the parts of the CME may be distorted or even rotated as they
 170 propagate from the Sun to 1 AU. “Fast” ICMEs, those propagating faster than the local
 171 upstream magnetosonic speed, result in the formation of interplanetary shocks antisunward of
 172 the CMEs. The shocks create downstream (sunward) interplanetary sheaths identified by
 173 compressed, heated and turbulent solar wind plasma and large amplitude magnetic field
 174 variations (Kennel et al., 1985; Tsurutani & Lin, 1985; Tsurutani et al., 1988). A subset of
 175 ICMEs are identified as MCs, with smooth magnetic field rotations and enhanced magnitudes,
 176 coupled with reduced proton temperatures and low plasma β s (Burlaga et al., 1981; Klein &
 177 Burlaga, 1982).

178

179 The solar wind HSSs emanating from CHs (Burlaga et al., 1978; Sheeley & Harvey, 1981) are
 180 identified in this paper with lower cutoff of speeds $V_{sw} > 550 \text{ km s}^{-1}$. The CIRs are identified
 181 in the interaction region between HSSs and slow ($V_{sw} \sim 300\text{-}400 \text{ km s}^{-1}$) streams as
 182 characterized by high plasma densities, temperatures and magnetic field amplitudes as
 183 mentioned previously.

184

185 *Magnetic storms, SSSs and GICs*

186

187 The symmetric ring current SYM-H indices (Sugiura, 1964; Wanliss & Showalter, 2006) are
 188 obtained from the World Data Center for Geomagnetism, Kyoto, Japan ([http://wdc.kugi.kyoto-
 189 u.ac.jp/](http://wdc.kugi.kyoto-u.ac.jp/)). These indices will be used to identify and study geomagnetic storms. The auroral
 190 SME and SML indices (Gjerloev, 2009) are based on ~300 ground-based magnetometer data
 191 taken from the SuperMAG network (<http://supermag.jhuapl.edu/>). The indices indicate auroral
 192 activity levels. Supersubstorms are defined as those events with peak SML < -2500 nT
 193 (Tsurutani et al., 2015; Hajra et al., 2016). The geomagnetically induced currents (GICs)
 194 measured in the natural gas pipeline near Mäntsälä, Finland (geographic: 60.6°N, 25.2°E)
 195 (Pulkkinen et al., 2001; Viljanen et al., 2006) are available from the Space and Earth
 196 Observation Centre of the Finnish Meteorological Institute (<http://space.fmi.fi/>). These GIC
 197 data are used in this study.

198

199 *Relativistic electrons*

200

201 To study the outer zone radiation belt dynamics during this month-long space weather interval,
 202 relativistic electron variations of the 2.00-7.15 MeV electron fluxes measured by the
 203 Relativistic Electron-Proton Telescope (REPT) instrument onboard the NASA Van Allen
 204 Probes (VAPs: Kessel et al., 2013; Mauk et al., 2013) are used. The data can be obtained at
 205 <http://vanallenprobes.jhuapl.edu/index.php>. The > 0.8 MeV and > 2.0 MeV electrons measured
 206 by the Energetic Proton, Electron, and Alpha Detector (EPEAD) instrument onboard GOES 15
 207 stationed at geosynchronous (L ~6.6) orbit will also be used in this part of the study
 208 (<https://www.goes.noaa.gov/>).

209

210 **3. Results**

211

212 **3.1. Major solar flares during September 2017**

213

214 Figure 1 shows the X-ray fluences at 1-8 Å and 0.5-4 Å wavelength ranges from GOES/SXI
 215 from 1 through 30 September 2017. A large number of solar flares were recorded, among which
 216 4 were X-class and 27 were M-class flares. This extreme solar flare activity was attributed to
 217 the extremely rapid development and increasing complexity of active region AR12673 that
 218 occurred during the AR passage over the Sun's western half of the visible disk (e.g., Chertok
 219 et al., 2018; Seaton & Darnel, 2018; Augusto et al., 2019).

220

221 The most powerful flares during the interval of study can be noted to occur during the first 5
 222 days of the month. The major ($> 10^{-4} \text{ W m}^{-2}$) X-flare (XFlare) details are listed in Table 1.

223

224 XFlare1 erupted at ~08:57 UT on 6 September and continued until ~09:17 UT. It attained its
 225 peak flux intensity (X2.2 flare) at ~09:10 UT. This flare eruption originated from AR12673
 226 around the equatorial region on the Sun's west limb (S08W33).

227

228 XFlare2 erupted at ~11:53 UT on 6 September had a peak flux intensity of X9.3 at ~12:02 UT.
 229 It continued until ~12:10 UT. This was the strongest flare of the month as well as being the
 230 most intense event of SC 24.

231

232 At ~14:20 UT on 7 September XFlare3 occurred when AR12673 moved closer to the western
 233 limb (S11W49). The flare attained its peak flux at ~14:36 UT and ended at ~14:55 UT.

234

235 XFlare4 had an intensity of X8.2. It erupted at ~15:35 UT on 10 September from AR12673
 236 when it was in the extreme western limb (S14W74). The flare attained its peak flux at ~16:06
 237 UT and ended at ~16:31 UT.

238

239 **3.2. CME propagation**

240

241 During September 2017 the SOHO/LASCO coronagraph detected ~68 CMEs which were
 242 associated with AR12673. Four of the CMEs were halo events directed towards the Earth. In
 243 Table 2 we have listed the halo CMEs (hCMEs) and their estimated speeds near the Sun. The
 244 estimated arrival times based on empirical models (Mod1, Mod2, Mod3) are also shown and
 245 compared with the actual observations of the interplanetary counterparts/fast shocks.

246

247 hCME1 erupted at ~20:36 UT on 4 September was associated with a M5.5 flare that started at
 248 ~20:28 UT, attained peak intensity at ~20:33 UT and ended at ~20:37 UT (not shown). For this
 249 halo CME, an interplanetary fast forward shock was detected at ~1 AU by the WIND spacecraft

250 at ~23:02 UT on 6 September. The three models predicted earlier arrivals of the hCME1 by
 251 ~11 h, 13 h and ~3 h, respectively, compared to the actual shock detection.

252
 253 The best predictions were found for the hCME2 that erupted at ~12:24 UT on 6 September in
 254 association with the X9.3-class flare (XFlare2, Table 1). The models Mod1, Mod2 and Mod3
 255 predicted the CME arrival times at 1 AU at ~22:48 UT on 7 September, at ~21:36 UT on 7
 256 September and at ~04:34 UT on 8 September, respectively. The actual fast forward shock
 257 detection by the WIND spacecraft was at ~22:19 UT on 7 September. Thus, the predicted
 258 arrival times are delayed by ~24 min by Mod1, occurs ~36 min earlier in Mod2, and is ~6 h 18
 259 min delayed by Mod3. One could say that all three predictions were reasonably accurate for
 260 this CME event. Since the CME prediction is not the shock time prediction, these results are
 261 quite accurate.

262
 263 hCME3 erupted at ~16:00 UT on 10 September near Sun arrived at ~1 AU (WIND) at ~19:12
 264 UT on 12 September. This CME was associated with the second strongest (X8.2) flare of
 265 September (XFlare4, Table 1). However, the three models predicted > 35 h earlier arrivals of
 266 the CME. It may be mentioned that the near-Sun CME speed was exceptionally high (3163 km
 267 s⁻¹) for this event. Any possible error in speed measurement might be associated with this large
 268 prediction error.

269
 270 For the hCME4 event launched from the Sun at ~12:00 UT on 17 September, no C-class or
 271 higher flare was detected by GOES/SXI. The models Mod1, Mod2 and Mod3 predicted arrivals
 272 of the CME at 1 AU at ~04:19 UT, ~02:10 UT and ~13:12 UT on 19 September, respectively.
 273 However, no significant interplanetary signature was detected in the WIND interplanetary data.
 274 Thus, although this was a halo CME, deflection or some other effect must have happened so
 275 that it missed the Earth.

276
 277 From the above discussion, it may be noted that the solar flares XFlare2 and XFlare4 were
 278 associated with the halo CMEs: hCME2 and hCME3, respectively. However, no halo CMEs
 279 were erupted in association with XFlare1 and XFlare3. XFlare1 was found to be associated
 280 with a CME which erupted at ~09:48 UT on 6 September with a central position angle (CPA)
 281 of 245° and an apparent angular width of ~80°. The CME with a liner speed of ~391 km s⁻¹
 282 near the Sun slowed down at a rate of ~-13.8 m s⁻² within the SOHO/LASCO field of view. On
 283 the other hand, XFlare3 was associated with a CME which erupted at ~15:12 UT on 7
 284 September. The CME, with an initial linear speed of ~433 km s⁻¹ near the Sun, slowed down
 285 at a rate of ~-9.9 m s⁻². None of these two CMEs arrived at the Earth as far as the authors could
 286 determine.

287 3.3. Interplanetary discontinuities and their geomagnetic effects

289
 290 Figure 2 shows an overview plot of the solar wind plasma, IMFs, and geomagnetic variations
 291 during September 2017. The major interplanetary events are marked. Eleven major
 292 interplanetary discontinuities are identified. Among them, 6 were fast forward shocks
 293 (indicated by red solid vertical lines), 2 were reverse waves (red dashed vertical lines), and 3
 294 were HCSs (green solid vertical lines). The interplanetary characteristics and associated
 295 geomagnetic impacts of the discontinuities are listed in Table 3. These will be discussed below.

296 *Fast forward shocks*

297
 298

299 During 6 of the 11 discontinuities, the solar wind speed V_{sw} , plasma density N_{sw} , ram pressure
 300 P_{sw} , temperature T_{sw} , and IMF amplitude B_0 all increased abruptly from upstream
 301 (antisunward) to downstream (sunward) of the discontinuities. These were identified as fast
 302 (magnetosonic) shocks propagating in the antisolar (forward) direction. These are marked
 303 sequentially as FS1 to FS6 in Figure 2 and Table 3. The shocks propagate with speeds larger
 304 than the upstream magnetosonic speed, thus they all have magnetosonic Mach numbers
 305 (MMNs) greater than 1.0 (by definition). Fast forward shocks have downstream density
 306 compressions that are approximately equal to the Mach number for low Mach number shocks
 307 ($MMN < 4$) and maximum compression of ~ 4 for high Mach number shocks ($MMN > 4$)
 308 (Kennel et al., 1985; Tsurutani et al., 2011). Thus, when the shock/sheath impacts the Earth's
 309 magnetosphere, a strong compression takes place which can lead to several types of different
 310 magnetospheric space weather effects. Among 6 fast forward magnetosonic shocks detected
 311 by the WIND spacecraft, 3 (FS1, FS2 and FS3) were associated with Earth-directed halo
 312 CMEs, and 3 (FS4, FS5 and FS6) were associated with CIRs followed by HSSs.

313
 314 FS1 occurred at $\sim 23:02$ UT on 6 September was associated with hCME1 which erupted on 4
 315 September (Table 2). The shock was found to propagate at ~ 5.8 times of the magnetosonic
 316 speed in the perpendicular direction ($\theta_{Bn} \sim 90^\circ$) to the ambient IMF. This unusual purely
 317 perpendicular shock, with a ram pressure P_{sw} increase of a factor of ~ 7 , caused a major sudden
 318 impulse (SI^+) of $\sim +56$ nT. The SI^+ occurred at $\sim 00:46$ UT on 7 September and is noted in the
 319 SYM-H index panel.

320
 321 FS2 detected at $\sim 22:19$ UT on 7 September was associated with hCME2 on 6 September (Table
 322 2). The shock was estimated to be propagating at ~ 6.7 times of the magnetosonic speed at an
 323 angle of $\sim 48^\circ$ relative to the IMF, and was characterized by a factor of ~ 5 increase in P_{sw}
 324 leading to a SI^+ of $\sim +20$ nT at $\sim 23:03$ UT. It also triggered an intense auroral supersubstorm
 325 (SSS1) (Tsurutani et al., 2015) with peak SME and SML intensities of 4464 nT and -3712 nT,
 326 respectively, at $\sim 00:24$ UT on 8 September. This supersubstorm will be discussed in more
 327 detail later in Section 3.6.

328
 329 FS3 occurred at $\sim 19:12$ UT on 12 September. FS3 was associated with the hCME3 on 10
 330 September (Table 2). The shock was found to be quasi-parallel in nature with $\theta_{Bn} \sim 19^\circ$, moving
 331 with a speed ~ 4 times the upstream magnetosonic speed. Even though the shock was quasi-
 332 parallel, it was characterized by a P_{sw} jump by a factor of ~ 8 and caused a SI^+ of $\sim +27$ nT at
 333 $\sim 20:09$ UT. FS3 triggered a moderate substorm with SME and SML peaks of 1366 nT and -
 334 1071 nT, respectively. These substorm peaks occurred at $\sim 21:04$ UT on 12 September.

335
 336 The fast forward shocks FS4, FS5 and FS6 (Figure 2 and Table 3) were detected at $\sim 00:00$ UT
 337 on 14 September, at $\sim 10:05$ UT on 14 September, and at $\sim 22:48$ UT on 26 September,
 338 respectively. All three shocks occurred at the leading (antisolar) edges of the CIRs (to be
 339 discussed in more detail later in Section 3.5).

340
 341 FS4 was determined to be quasi-parallel, moving at ~ 4.3 times of the upstream magnetosonic
 342 speed at an angle $\sim 9^\circ$ relative to the ambient IMF. It was characterized by a factor of ~ 4 ram
 343 pressure P_{sw} jump resulting in a SI^+ $\sim +14$ nT at $\sim 01:31$ UT on 14 September.

344
 345 FS5 was quasi-perpendicular ($\theta_{Bn} \sim 84^\circ$) in nature and was a Mach ~ 1.7 shock. A ramp pressure
 346 P_{sw} jump by a factor of ~ 4.5 led to a SI^+ $\sim +28$ nT which occurred at $\sim 12:12$ UT on 14
 347 September.

348

349 FS6 was determined to propagate at ~ 2.7 times of the upstream magnetosonic speed at an angle
 350 of $\sim 34^\circ$ relative to the ambient IMF. A SI^+ of $\sim +14$ nT was induced at $\sim 23:55$ UT on 26
 351 September by a ram pressure P_{sw} jump of ~ 3 across this shock.

352

353 FS4, FS5 and FS6 did not trigger substorms. This may have to do with precursor interplanetary
 354 magnetic fields being mostly northward.

355

356 *Reverse waves*

357

358 Two of the 11 discontinuities were characterized by V_{sw} increases with the other parameters
 359 (N_{sw} , P_{sw} , T_{sw} , B_o) simultaneously decreasing with time. In addition, these were determined
 360 to be moving at submagnetosonic speeds, indicating that they were not shocks, but reverse
 361 waves (RWs). By “reverse” we mean that the waves were propagating towards the Sun but
 362 because the solar wind speed is higher than the speed of the waves, the waves were convected
 363 in the antisolar direction. These two waves are marked by RW1 and RW2 in Figure 2 and Table
 364 3.

365

366 RW1 at $\sim 18:29$ UT on 14 September was determined to have speed $\sim 84\%$ of the upstream
 367 (sunward) magnetosonic speed. The angle of propagation was $\sim 71^\circ$ relative to the ambient
 368 IMF. The ram pressure P_{sw} decreased with time across RW1 by a factor of $\sim 1/7$. Thus, when
 369 RW1 impacted the Earth’s magnetosphere, it caused a decompression of the magnetosphere,
 370 opposite to what happens when a forward shock/wave impacts the magnetosphere. RW1 caused
 371 a negative sudden impulse (SI) of ~ -23 nT at $\sim 21:08$ UT on 14 September. RW1 also caused
 372 a substorm recovery as seen from an increase in SML index from a value of ~ -584 nT at $\sim 18:40$
 373 UT to ~ -133 nT at $\sim 19:40$ UT.

374

375 RW2 occurred at $\sim 08:38$ UT on 28 September and had a speed $\sim 71\%$ of the upstream
 376 magnetosonic speed. It was propagating oblique to the ambient magnetic field at an angle of
 377 $\sim 87^\circ$. The ram pressure P_{sw} decreased by a factor of $\sim 1/3$ across the RW2. It caused a SI of
 378 ~ -14 nT at $\sim 09:37$ UT on 28 September. RW2 was associated with a substorm recovery phase
 379 as seen in SML decrease from ~ -813 nT at $\sim 09:31$ UT to ~ -198 nT at $\sim 10:04$ UT.

380

381 *HCSs and HPSs*

382

383 The HCS crossings represent tangential discontinuities where the IMF B_x and B_y exhibit
 384 simultaneous polarity/sign reversals. Three HCSs detected during this study are marked as
 385 HCS1, HCS2 and HCS3 in Figure 2 and Table 3.

386

387 HCS1 occurred at $\sim 14:10$ UT on 14 September. It was characterized by simultaneous positive-
 388 to-negative B_x and negative-to-positive B_y polarity reversals. By convention (Ness & Wilcox,
 389 1964), magnetic fields pointed outward from the Sun have a “positive” polarity. A peak plasma
 390 density of ~ 40 cm^{-3} was associated with HPS1. It triggered a moderate substorm with peak
 391 SML intensity of -766 nT and SME intensity of 1171 nT at $\sim 15:41$ UT.

392

393 HCS2 occurred at $\sim 21:22$ UT 24 September, characterized by negative-to-positive B_x and a
 394 positive-to-negative B_y polarity reversals. HPS2 had a peak plasma density of ~ 36 cm^{-3} . No
 395 substorm was triggered by HPS2.

396

397 HCS3 occurring at $\sim 05:17$ UT on September 27 exhibited a simultaneous positive-to-negative
 398 B_x and a negative-to-positive B_y polarity reversal. The associated HPS3 had a peak density of

399 $\sim 54 \text{ cm}^{-3}$. It triggered a substorm with peak SML intensity of -614 nT and SME intensity of
 400 883 nT at $\sim 07:39 \text{ UT}$.

401

402 In addition to the interplanetary discontinuities described above, the interplanetary space
 403 during September 2017 was characterized by interplanetary sheaths, ICMEs, and CIRs. The
 404 detailed case-by-case analyses of the interplanetary events, their characteristics and
 405 geomagnetic impacts will be presented next in the Sections 3.4 – 3.7.

406

407 **3.4. Interplanetary sheaths, ICMEs and their geomagnetic effects**

408

409 In this section, we study the interplanetary sheaths and MCs identified during September 2017,
 410 and their geomagnetic impacts. The event durations and their major impacts are listed in Table
 411 4.

412

413 *Interplanetary events during 6 – 11 September*

414

415 Figure 3 shows interplanetary events and associated geomagnetic impacts during 6 – 11
 416 September 2017. Two interplanetary sheaths were detected during this period. Sheath1
 417 extended from FS1 at $\sim 23:02 \text{ UT}$ on 6 September to FS2 at $\sim 22:19 \text{ UT}$ on 7 September. Sheath2
 418 followed FS2 at $\sim 22:19 \text{ UT}$ on 7 September to $\sim 11:02 \text{ UT}$ on 8 September (Table 4). The
 419 sheaths are marked by green horizontal bars on the top of Figure 3. These were characterized
 420 by large IMF Bz fluctuations with peak southward Bz components of $\sim 11 \text{ nT}$ at $05:51 \text{ UT}$ and
 421 $\sim 31 \text{ nT}$ at $\sim 23:02 \text{ UT}$ on 7 September, respectively. Sheath1 was comparatively less
 422 geoeffective, associated SYM-H peak was only -15 nT . A moderate substorm with SME and
 423 SML peak intensities of 1417 nT and -1097 nT , respectively at $\sim 09:05 \text{ UT}$ was recorded during
 424 Sheath1. The southward Bz associated with Sheath2 caused a sharp decrease in SYM-H index
 425 with peak magnetic storm intensity of -146 nT at $\sim 01:10 \text{ UT}$ on 8 September (intense magnetic
 426 storm, IMS1: Gonzalez et al., 1994). The storm main phase was associated with a long-duration
 427 ($\sim 3.2 \text{ h}$) southward component of the Sheath2 IMF. The SSS1 in this magnetic storm main
 428 phase (mentioned previously) was triggered by FS2, while the Sheath2 southward field appears
 429 to have acted as the energy source for the SSS1.

430

431 Sheath2 was followed by a MC, which occurred from $\sim 11:02 \text{ UT}$ on 8 September through
 432 $\sim 00:43 \text{ UT}$ on 11 September (Table 4). This is marked by a red horizontal bar at the top of
 433 Figure 3. The MC is identified by low plasma β ($\sim 2 \times 10^{-2}$), low Tsw ($\sim 4 \times 10^4 \text{ K}$), a negative-to-
 434 positive rotation in Bx, and a south-to-zero Bz configuration. The initial southward IMF
 435 component lasted $\sim 3.7 \text{ h}$ with peak negative Bz intensity of -17 nT at $\sim 11:22 \text{ UT}$ on 8
 436 September. This southward Bz was responsible for development of the main phase of the
 437 second intense storm (IMS2). This had a peak SYM-H intensity of -115 nT at $13:56 \text{ UT}$ on 8
 438 September. This interval was also associated with an SSS (SSS2) with SME and SML peak
 439 intensities of 4330 nT and -2642 nT , respectively. The peak SSS2 intensity occurred at $\sim 13:08$
 440 UT on 8 September. The SSS2 will be discussed latter in more detail in Section 3.6.

441

442 *Interplanetary events during 12 – 13 September*

443

444 Interplanetary events and resultant geomagnetic activity during 12 – 13 September are shown
 445 in Figure 4. The interplanetary variations following FS3 (associated with hCME3) indicate
 446 some unclear events. The interval from $\sim 19:12 \text{ UT}$ on 12 September to $\sim 03:22 \text{ UT}$ on 13
 447 September is characterized by large IMF fluctuations with southward Bz components lasting
 448 for $\sim 25 \text{ min}$, $\sim 28 \text{ min}$, $\sim 26 \text{ min}$ and $\sim 43 \text{ min}$ durations with peak intensities of $\sim 8 \text{ nT}$, $\sim 8 \text{ nT}$,

449 ~-12 nT and ~-11 nT, respectively. This possibly may be indicative of an interplanetary sheath
 450 (marked as Sheath3, Table 4). This will be further discussed in the discussion section. The
 451 Sheath3 led to a moderate magnetic storm (MMS1) with SYM-H peak intensity of -65 nT at
 452 ~00:12 UT on 13 September.

453
 454 Two auroral substorms were detected during this interval. One substorm had peak SME and
 455 SML indices of 1366 nT and -1071 nT, respectively, at ~21:04 UT, and the other had peak
 456 SME and SML intensities of ~1856 nT and ~-1541 nT, respectively at ~23:57 UT on 12
 457 September.

458
 459 Sheath4 occurred between FS4 and FS5, from ~00:00 UT to ~10:05 UT on 14 September. This
 460 had only weak IMF Bz southward component of ~-4 nT. While no magnetic storm was detected
 461 during this interval, auroral activity had peak SME and SML intensities of 389 nT and -306 nT
 462 at ~05:29 UT on 14 September.

463

464 **3.5. Interplanetary HSSs, CIRs and their geomagnetic effects**

465

466 From the variations of solar wind plasma speed V_{sw} , 3 HSSs were identified (see Figure 2).
 467 CIRs were identified as the compressed plasma and magnetic fields in the interaction regions
 468 between low-speed streams and HSSs. It may be noted that the CIR event associated with HSS1
 469 occurred before 1 September, so this was not included in the present analysis. The HSS and
 470 CIR event intervals, their V_{sw} characters and major impacts are listed in Table 5.

471

472 *HSSs*

473

474 HSS1 had a peak plasma speed V_{sw} of ~687 km s⁻¹ at ~15:00 UT on 1 September (Table 5).
 475 This event extended to approximately the end of 2 September. The SDO/AIA telescope
 476 identified a large coronal hole (CH25) on 28 August as the source of this HSS (not shown).
 477 Coronal hole CH25 had a positive magnetic polarity (defined as the magnetic field pointing
 478 away from the Sun) and extended from the solar north pole down to ~+5° latitude around ~180°
 479 Carrington longitude. No magnetic storm was recorded in SYM-H (the peak SYM-H was -28
 480 nT). Discrete multiple southward components (~-5 nT) of an Alfvén wave train embedded
 481 within the HSS1 proper resulted in intense auroral activity, with peak SME and SML intensities
 482 of ~1588 nT and ~-1439 nT, respectively. However, this was not an “ideal” high-intensity
 483 (SME peak > 1000 nT), long-duration (≥ 2 days), continuous (SME never dropping below 200
 484 nT for > 2 h at a time) auroral electrojet activity (HILDCAA) event defined by Tsurutani &
 485 Gonzalez (1987). Although there was a peak SME value of > 1000 nT and the event lasted for
 486 > 2 days, the SME decreased below 200 nT for > 2 h several times within the interval.

487

488 HSS2 emanated from a coronal hole (CH30) with positive magnetic polarity, extending from
 489 the solar north pole down to ~+15° latitude with a Carrington longitude extent of ~80° to ~240°,
 490 identified on 14 September. HSS2 had a peak V_{sw} of ~743 km s⁻¹ at ~06:36 UT on 15
 491 September (Table 5). It lasted approximately to the end of 18 September. HSS2 was associated
 492 with long-duration IMF Bz fluctuations (peak southward Bz ~-6.6 nT) indicating an Alfvén
 493 wave train leading to intense auroral activity as observed in peak SME (~1749 nT) and peak
 494 SML (-1423 nT) indices. However, this was again not an “ideal” HILDCAA event. The SME
 495 decreased below 200 nT for > 2 h several times. The SYM-H peak intensity was -44 nT,
 496 registering no geomagnetic storm.

497

498 HSS3 emanated from a positive magnetic field coronal hole (CH32) on 26 September
 499 (extending from north pole of the Sun down to $\sim -10^\circ$ latitude at around $\sim 190^\circ$ Carrington
 500 longitude). This HSS impacted the Earth's magnetosphere from 27 to 29 September (Table 5).
 501 It had a peak V_{sw} of $\sim 721 \text{ km s}^{-1}$ at $\sim 11:41$ UT on 28 September. The HSS3 proper was
 502 characterized by intense auroral activity (peak SME $\sim 2044 \text{ nT}$, SML $\sim -949 \text{ nT}$) associated with
 503 Alfvén wave IMF Bz southward fields (peak $\sim -4 \text{ nT}$). However, HSS3 did not lead to a
 504 magnetic storm (SYM-H peak = -43 nT).

505

506 *14 September CIR (CIR1)*

507

508 Figure 5 shows the interplanetary events during 13 – 19 September and associated geomagnetic
 509 impacts. Following Sheath4, a CIR was identified from $\sim 10:05$ UT to $\sim 18:29$ UT on 14
 510 September (CIR1). This was characterized by a plasma density (N_{sw}) enhancement from ~ 6
 511 to $\sim 56 \text{ cm}^{-3}$, and an IMF B_o enhancement from ~ 2 to $\sim 22 \text{ nT}$. The leading and trailing edges
 512 of the CIR1 were characterized by the fast forward magnetosonic shock FS5 and reverse wave
 513 RW1, respectively (Table 3). In addition, a tangential discontinuity HCS1 characterized the
 514 complex CIR1 event.

515

516 CIR1 did not cause a magnetic storm (SYM-H peak -19 nT). This was presumably because of
 517 the short-duration IMF southward components inside the CIR1. For example, two intervals of
 518 southward IMFs were detected with durations of ~ 38 min and ~ 56 min and peak Bz of ~ -19
 519 nT and -16 nT , respectively. While intensities of southward IMF were high, short durations
 520 indicate lesser amount of magnetospheric energy input which is not sufficient for a magnetic
 521 storm (Gonzalez et al., 1994).

522

523 *26 – 28 September CIR (CIR2)*

524

525 The interval from 23 to 30 September is illustrated in Figure 6. A CIR was identified from
 526 $\sim 22:48$ UT on 26 September to $\sim 08:38$ UT on 28 September (CIR2). The plasma density N_{sw}
 527 increased from ~ 12 to $\sim 59 \text{ cm}^{-3}$. The IMF B_o increased from ~ 3 to $\sim 17 \text{ nT}$. The fast forward
 528 shock FS6 and reverse wave RW2 were located at the leading and trailing edges of the CIR2,
 529 respectively (Table 3). The HCS3 was detected inside CIR2.

530

531 CIR2 caused a moderate intensity magnetic storm (MMS2). The storm was characterized by a
 532 gradual, multi-step main phase development with SYM-H peak intensity of -74 nT at $\sim 05:57$
 533 UT on 28 September. The southward component of Alfvénic IMF was responsible for this
 534 moderate storm. For example, southward IMF intervals of ~ 2 h, ~ 3.5 h, ~ 1.4 h and ~ 1.3 h were
 535 recorded with peak Bz of $\sim -15.4 \text{ nT}$, $\sim -11.3 \text{ nT}$, $\sim -10.5 \text{ nT}$ and $\sim -9.5 \text{ nT}$, respectively inside
 536 the CIR2. During the storm main phase, peak SME and SML intensities were 2683 nT and $-$
 537 1813 nT , respectively.

538

539 **3.6. SSSs and GIC effects**

540

541 Two SSSs (SML $< -2500 \text{ nT}$) were detected during September 2017. These occurred on 7-8
 542 September (Figure 3). They were found to induce strong GICs in the Finnish natural gas
 543 pipeline. The SSS characters and associated GIC recordings are summarized in Table 6.

544

545 SSS1 started at $\sim 22:19$ UT on 7 September preceded by an IMF southward turning at $\sim 19:30$
 546 UT. The SSS energy loading was associated with Sheath1 southward field with peak Bz
 547 component of $\sim -31 \text{ nT}$ at $\sim 23:02$ UT on 7 September. It was triggered by the fast forward shock

548 FS2 (Table 3). The SSS attained its peak SML intensity of -3712 nT at ~00:24 UT and ended
 549 at ~02:51 UT on 8 September. It had a total duration of ~4 h 32 min. This SSS occurred in the
 550 main phase of an intense magnetic storm (IMS1) with SYM-H peak intensity of -146 nT, the
 551 SML peak occurring ~46 min earlier than the SYM-H peak (see Section 3.4). The SSS1
 552 recovery phase was associated with very intense GICs at the Finland station which at the time
 553 was in local postmidnight. The GIC had a peak eastward intensity of ~28 A at ~03:31 local
 554 time (LT = UT + 3 h).

555

556 SSS2 started at ~11:34 UT and ended at ~15:42 UT on 8 September, with a total duration of
 557 ~4 h 8 min. The SSS onset was preceded by an IMF southward turning at ~10:26 UT as a part
 558 of the MC1 and was triggered by a high ram pressure Psw region. This Psw region occurred
 559 from ~08:13 UT to ~11:14 UT with a peak Psw of ~8.5 nPa. The SSS was characterized by a
 560 peak SML intensity of -2642 nT at ~13:08 UT. This was preceded by an IMF precursor Bz
 561 peak of -17 nT at ~11:22 UT. SSS2 was also detected in the intense magnetic storm main phase
 562 which had a SYM-H intensity of -115 nT (IMS2). The SSS SML peak occurred ~48 min earlier
 563 than the SYM-H peak (Section 3.4). Large amplitude GICs occurred during the SSS2 recovery
 564 phase, with peak (eastward) component of ~30 A at ~20:55 LT.

565

566 **3.7. Outer zone radiation belt variation**

567

568 Responses of the outer zone radiation belt to the complex and multiple space weather events
 569 during 1 through 30 September are shown in Figure 7. Varying interplanetary and
 570 magnetospheric space weather events can be related to changes in the relativistic electron
 571 fluxes.

572

573 *Effects of interplanetary discontinuities on relativistic electron fluxes*

574

575 Figure 7 shows that at the GOES 15 geosynchronous orbit, the fast forward shock FS1 led to a
 576 relativistic > 0.8 MeV and > 2.0 MeV electron flux decrease by ~1 order of magnitude followed
 577 by a further ~1 order of magnitude decrease caused by the following fast shock FS2. The
 578 combination of the two shocks resulted in a net flux decrease of ~2 orders of magnitude from
 579 $\sim 990 \times 10^2$ to $\sim 450 \text{ cm}^{-2} \text{ sr}^{-1} \text{ s}^{-1}$ for > 0.8 MeV electrons, and from $\sim 90 \times 10^2$ to $\sim 90 \text{ cm}^{-2} \text{ sr}^{-1} \text{ s}^{-1}$
 580 for > 2.0 MeV electrons. This occurred during the main phase of the intense storms of 7 – 8
 581 September. The VAP L-shell observations show that the entire outer radiation belt was flux-
 582 depleted during this period. The flux depletions were most prominent around L ~4-5 for the 2-
 583 4.50 MeV electrons.

584

585 The combination of FS3, FS4 and FS5 (at the leading edge of the CIR1) depleted the outer
 586 zone radiation belt during 13 – 14 September. At the geosynchronous orbit the net flux decrease
 587 was ~2 orders of magnitude. From the VAPs L-shell flux observations, clear energy
 588 dependence can be noted. The strongest flux depletions were recorded at L > 5 for 2-2.30 MeV
 589 electrons, at L > 4.5 for 2.85 MeV electrons, and at L > 4 for ≥ 3.60 MeV electrons. No
 590 prominent magnetospheric impacts of the HPS1 and RW1 were apparent.

591

592 The outer zone (L > 4) magnetosphere relativistic electron belt was strongly depleted by the
 593 solar wind ram pressure pulses of HPS2, FS6 and HPS3 during 25 – 28 September. No
 594 prominent impacts were recorded owing to RW2.

595

596 *Effects of MC on relativistic electron fluxes*

597

598 The MC and the magnetic storm it induced (IMS1) was associated with large relativistic
 599 electron flux increases compared to pre-shock flux values. This increase was mainly for $L < 5$.
 600 Presumably the storm time convection electric field injected the energetic ~ 30 to 300 keV
 601 electrons deep into the magnetosphere with further particle energization by chorus wave
 602 interactions. Flux enhancements by > 2 orders of magnitude were noted around $L \sim 3-4$
 603 associated with the magnetic storm discussed in Section 3.4. Most interestingly, the low flux
 604 density slot region ($2 < L < 2.5$) separating the inner ($L < 2$) and outer ($L > 2.5$) radiation belts
 605 moved inward. The large amplitude flux enhancement during the storm recovery phase is
 606 interesting. This was characterized by intense auroral SME/SML substorm activity preceded
 607 by SSS2. Thus, this portion is most likely acceleration by chorus wave interactions.

608

609 *Effects of HSSs on relativistic electron fluxes*

610

611 HSS intervals are found to be characterized by IMF Alfvén wave trains and intense auroral
 612 SME/SML activities. The chorus wave generation by the temperature anisotropic $\sim 10-100$ keV
 613 electron injections are believed to accelerate the ~ 100 keV electrons to \sim MeV energies. It
 614 appears that HSS2 and HSS3 did indeed repopulated the radiation belt with $> 0.8-7.15$ MeV
 615 electrons. The largest flux enhancements were recorded around $L \sim 4-5.5$. It may be recollected
 616 that peak flux enhancements due to the MC were deeper into the magnetosphere, at $L \sim 3-4$.
 617 For the 2.85-7.15 MeV electrons, two separated belts can be identified during 16 – 27
 618 September: a radiation belt enhanced by the MC around $L \sim 3-3.5$ and an enhanced belt due to
 619 HSS2 around $L \sim 4-5$.

620

621 **4. Discussion**

622

623 September 2017 was an interesting period for complex and multiple space weather events
 624 occurring during a descending-to-minimum solar cycle phase. Extremely rapid development
 625 and increasing complexity of AR12673 resulted in eruptions of numerous class-C and above
 626 solar flares and CMEs. Multiple well-developed and extended CHs emitting HSSs contributed
 627 to space weather complexity during this period.

628

629 *Solar Flares and CMEs*

630

631 Out of four X-class, twenty-seven M-class and numerous C-class solar flares that occurred
 632 from AR12673 on the western limb, three were related to halo CMEs. Among the three flares
 633 causing halo CMEs, one was M-class (M5.5) and two were X-class (X9.3 and X8.2) flares. No
 634 C-class or above flare was associated with one halo CME. This may have been associated with
 635 a disappearing filament (Tang et al., 1989; Zhou et al., 2003; Lepri & Zurbuchen, 2010). On
 636 the other hand, two X-class (X2.2 and X1.3) flares did not have associated halo CMEs. These
 637 solar results are consistent with previous reports (e.g., Chertok et al., 2018; Redmon et al.,
 638 2018; Yan et al., 2018; Zou et al., 2019).

639

640 Among the four halo CMEs detected during this period, three arrived at 1 AU, as detected by
 641 fast forward shocks followed by sheaths and/or MC. However, no significant interplanetary
 642 signature was recorded at 1 AU during one halo CME. Deflections away from the straight line
 643 propagation during active interval or some other effects are suggested to happen so that it
 644 missed the Earth. We estimated the propagation times of halo CMEs from the Sun to Earth
 645 based on near-Sun CME speed measurement. We used an empirical CME arrival model
 646 (Gopalswamy et al., 2001) employing three different expressions for CME acceleration
 647 (Gopalswamy et al., 2001; Michalek et al., 2004) up to ~ 0.76 AU, after which the CME was

648 assumed to travel at a constant speed up to ~ 1 AU. The prediction errors varied from ~ 24 min
 649 to > 35 h with respect to the actual CME signatures detected by the WIND spacecraft (~ 1 AU).
 650 However, any possible error in near-Sun CME speed measurement can cause the above
 651 prediction errors. In addition, as previously discussed by Echer et al. (2009), modelling CME
 652 propagation delays during solar active intervals is difficult due to the complexity of the
 653 interplanetary medium. Codes that work for simple events may not be accurate during periods
 654 when multiple CMEs are being launched from the Sun.

655

656 *Magnetic Storms*

657

658 There were two intense (peak SYM-H ≤ -100 nT) and two moderate (-100 nT $<$ peak SYM-H
 659 ≤ -50 nT) magnetic storms during September 2017. None were at the superstorm level (SYM-
 660 H peak ≤ -250 nT). The intense storms (with peak SYM-H of -146 nT and -115 nT) occurred
 661 consecutively on 8 September. The first storm was caused by southward IMF Bz fields in the
 662 Sheath2. The second storm was caused by southward IMF Bz fields in the MC. A moderate
 663 storm (with peak SYM-H of -65 nT) was caused by another sheath (Sheath3) on 13 September.
 664 These three events were related to halo CMEs: hCME1, hCME2 and hCME3, respectively. As
 665 mentioned previously, Sheath3 represented an unclear event. This was not followed by a MC.
 666 We explored the possibility of this being a filament (Tang et al., 1989; Zhou et al., 2003; Lepri
 667 & Zurbuchen, 2010; Kozyra et al., 2014). However, filaments inside ICMEs are reported (e.g.,
 668 Lepri & Zurbuchen, 2010) to be low-temperature. The present event (Sheath3) was determined
 669 to be a sheath due to its high temperature in addition to compressed and turbulent plasma and
 670 IMF features. For hCME4 no clear interplanetary signature and geomagnetic impact were
 671 identified at the Earth. The second moderate storm (peak SYM-H of -74 nT) on 27-28
 672 September was associated with the CIR2 event. CIR1 on 14 September did not cause any
 673 magnetic storm.

674

675 No magnetic storms were caused by three HSS events detected in this study. However, they
 676 led to intense (peak SME ~ 1588 nT, ~ 1749 nT, ~ 2044 nT) and continuous auroral activity for
 677 several days. While long-duration (> 3 h), intense southward IMFs in the sheaths and the MC
 678 led to intense magnetic storms, short-duration (< 1 h), sporadic southward components within
 679 the CIRs and HSSs caused only moderate magnetic storms with peak SYM-H > -100 nT.
 680 However, as expected, the short duration IMF Bz components caused intense, long-duration
 681 auroral activity. These are consistent with present understanding of geoeffectiveness of
 682 interplanetary events like ICMEs, CIRs and HSSs (e.g., Tsurutani & Gonzalez, 1987; Tsurutani
 683 et al., 1988, 1995, 2006; Gonzalez et al., 1994; Zhang et al., 2007; Echer et al., 2008; Hajra et
 684 al., 2014; Meng et al., 2019).

685

686 Studies on the intense storm of 8 September were reported previously (e.g., Berdermann et al.,
 687 2018; Clilverd et al., 2018; Shen et al., 2018; Augusto et al., 2019). The storm was attributed
 688 to the combined interplanetary shock-ICME events, which corroborates with the present
 689 analysis.

690

691 *Sudden impulses, substorm triggers and recoveries*

692

693 There were six FSs with Mach numbers ranging from ~ 1.7 to ~ 6.7 and with planar normal
 694 oriented at $\sim 9^\circ$ to $\sim 90^\circ$ relative to the ambient upstream magnetic field direction. All FSs
 695 caused SI⁺s ranging from $\sim +14$ nT to $\sim +56$ nT. Two of the FSs triggered substorms. There
 696 were three HCSs characterized by simultaneous IMF Bx, By polarity changes. The associated
 697 HPS pressure pulses triggered substorms. Substorm triggering by FS/HPS pressure pulses was

698 noted to be preceded by IMF southward turning indicating magnetospheric energy preloading.
 699 Two quasi-perpendicular RWs moving at submagnetosonic speeds were detected. Both
 700 initiated substorm recoveries.

701

702 *Supersubstorms and GIC effects*

703

704 Two SSSs were detected during September 2017. These were preceded (~2.8 h and ~1.1 h) by
 705 precursor southward IMFs. SSSs were triggered by solar wind ram pressure pulses. Analysis
 706 of current measurements in Finnish natural gas pipeline indicates that the SSSs led to large
 707 GICs in the local dusk and postmidnight sectors. The GICs are known to be related to large
 708 dB/dt variations (e.g., Pirjola, 2000; Viljanen et al., 2001; Boteler, 2003). It may be noted that
 709 there are previous reports of ground electrical anomalies and/or power outages occurring
 710 during magnetic storms (e.g., Loomis, 1861; Allen et al., 1989; Lanzerotti, 1992). Magnetic
 711 storm ring current intensifications are unlikely to directly impact ground power grid systems.

712

713 *Outer zone relativistic electrons*

714

715 It was shown that substantial outer zone magnetospheric relativistic electron fluxes decreased
 716 when interplanetary FSs and HCSs/HPSSs impinged on the magnetosphere. Tsurutani et al.
 717 (2016) showed that HPSSs caused non-storm relativistic electron flux decreases. Hajra &
 718 Tsurutani (2018b) showed that FSs can also cause flux decreases. The scenario is that solar
 719 wind pressure pulses cause the generation of coherent electromagnetic ion cyclotron (EMIC:
 720 Cornwall, 1965; Kennel & Petschek, 1966) waves in the dayside magnetosphere. These waves
 721 can have parasitic resonant interaction with relativistic electrons, causing their pitch angle
 722 scattering and loss to the atmosphere (Thorne & Kennel, 1971; Meredith et al., 2003; Summers
 723 et al., 2007; Remya et al., 2015; Tsurutani et al., 2016). However, there is another possibility
 724 of a relativistic electron loss mechanism, that of “magnetopause shadowing” where the
 725 electrons gradient drift to the magnetopause and are lost into the solar wind (West et al., 1972;
 726 Li et al., 1997; Hudson et al., 2014). At this time, it is uncertain which of the two mechanisms
 727 dominate. It seems quite likely that both are occurring. It is possible that the dominant effect
 728 may vary from case to case. Further research on this topic is needed.

729

730 Relativistic electron flux enhancements were recorded during the HSS intervals and the MC
 731 associated with the magnetic storm recovery phase. The largest flux enhancements during the
 732 HSSs were recorded around L ~4-5.5. However, the peak flux enhancements owing to the MC
 733 induced storm convection were deeper into the magnetosphere, at L ~3-4. In addition, during
 734 the MC event, the slot region separating the inner ($L < 2$) and outer ($L > 2.5$) radiation belts
 735 occurred at lower L. These results corroborate with previous results (Baker et al., 2014;
 736 Kanekal et al., 2015). Tsurutani et al. (2018) have speculated that the electron slot is created
 737 by coherent chorus waves propagating into the plasmasphere and interacting with the
 738 relativistic electrons. This new mechanism will cause rapid loss of the electrons during the
 739 chorus (substorm/storm) event.

740

741 **5. Summary and Conclusion**

742

743 We explored the solar, interplanetary and geomagnetic events occurring during September
 744 2017. This interval was in a descending-to-minimum phase of a solar cycle. The main results
 745 are summarized below.

- 746 1. There were 4 X-class, 27 M-class and a myriad of C-class flares and ~68 CME eruptions
747 from solar active region AR12673. Only 4 halo CMEs were detected, among them 3
748 reached the Earth, and 1 did not reach the Earth.
- 749 2. The two strongest flares (X9.3 and X8.2) of the present study were associated with two
750 halo CMEs. A third halo CME was associated with a M5.5 flare. No solar flare was
751 detected during the fourth halo CME. Thus, a complex relationship between flares and
752 halo CMEs is indicated.
- 753 3. Six fast forward magnetosonic shocks (FSs) were detected (Figure 2, Table 3). Half of
754 them were associated with halo CMEs (Table 2) and half were detected at the leading
755 antisolar edges of CIRs. The angle of propagation (θ_{Bn}) of the FSs varied from $\sim 9^\circ$ to
756 $\sim 90^\circ$ relative to the ambient IMFs, while their strengths varied from Mach ~ 1.7 to Mach
757 ~ 6.7 . The induced SI^+ strengths varied between $\sim +14$ nT to $\sim +56$ nT. Two CME FSs
758 triggered substorms. None of the CIR FSs triggered substorms due to a lack of prior
759 southward IMF conditioning. The FS impingements on the magnetosphere led to large
760 MeV electron flux depletions in the Earth's outer radiation belt ($L > 4$) (Figure 7).
- 761 4. Two non-shock reverse waves (RWs) were detected at the trailing edges of the CIRs
762 (Figure 2, Table 3). They were found to be propagating mostly across the magnetic field
763 ($\theta_{Bn} \sim 71^\circ$ - 88°) at submagnetosonic (~ 71 - 88%) speeds. Both RWs caused negative
764 sudden impulses SI^- ~ -14 to -23 nT and both caused the termination of ongoing
765 substorms. There were no reverse shocks detected in this study.
- 766 5. Three HCSs were detected (Figure 2, Table 3). HPSs adjacent to two of them triggered
767 moderate intensity substorms. All three high pressure pulses associated with the HPSs
768 led to relativistic electron flux decreases in the outer radiation belt.
- 769 6. Southward IMFs associated with an interplanetary sheath and the following MC led to
770 two intense consecutive magnetic storms with peak SYM-H intensities of -146 nT and
771 -115 nT, respectively (Figure 3, Table 4). Two moderate storms with peak SYM-H of
772 -65 nT and -74 nT were caused by southward IMFs associated with another sheath and
773 a CIR event (Figures 4, 6, Tables 4, 5). The MC and the magnetic storm led to
774 relativistic electron flux enhancements (Figure 7). The peak flux enhancements were
775 noted deep within magnetosphere ($L \sim 3$ - 4). In addition, the low flux density slot region
776 ($2 < L < 2.5$) separating the inner ($L < 2$) and outer ($L > 2.5$) radiation belts moved
777 inward.
- 778 7. Two SSSs (with peak SML intensities of -3712 nT and -2642 nT) occurred in the main
779 phases of the intense magnetic storms. The SSSs were preceded (~ 2.8 h and ~ 1.1 h) by
780 precursor southward IMFs followed by solar wind ram pressure pulse triggering. SSSs
781 were associated with large GICs with peak values of ~ 28 A and ~ 30 A recorded in the
782 local (Finland) postmidnight and dusk sectors, respectively (Table 6).
- 783 8. Two CIRs were characterized by fast magnetosonic shocks bounding the leading
784 antisolar edges and reverse submagnetosonic waves at the trailing edges (Figures 5, 6,
785 Table 5). Weak and short duration southward IMFs in a CIR led to a moderate magnetic
786 storm with SYM-H peak of -74 nT. However, the other CIR did not lead to a magnetic
787 storm but small ring current activity (SYM-H peak = -28 nT) and high level (peak SME
788 > 1000 nT) auroral zone activity.
- 789 9. HSSs were associated with intense auroral activities indicated by the SME and SML
790 indices. However, these were not HILDCAAs in the strict definition. The HSSs did not
791 cause magnetic storms (with SYM-H < -50 nT). The HSSs were associated with
792 relativistic electron flux enhancements prominently around $L \sim 4$ - 5.5 (Figure 7).
- 793 10. We estimated the probable halo CME arrival times at ~ 1 AU from the Sun using an
794 CME arrival model and three different expressions for CME acceleration in the
795 interplanetary space (Table 2). The prediction error varied from ~ 24 min to > 35 h with

796 respect to the actual CME signatures detected by the WIND spacecraft. The efficiency
797 of the individual models is found to vary from one event to the other.

798

799 In general, we have found nothing particularly unusual in resultant geomagnetic activity in this
800 solar minimum interval than what occurs during solar maximum. All of the basic known solar
801 wind effects on geomagnetic activity can be applied. Perhaps the occurrence of simultaneous
802 HSSs is one small complexity. However, the addition of HSSs only led to auroral zone
803 HILDCAA-like activity and the acceleration of magnetospheric relativistic electron fluxes. The
804 formation of the AR in this solar cycle minimum phase is the source for the halo CMEs and
805 potential magnetic storms. Thus, it will be the goal of the solar physicists to tell us when ARs
806 occur during this phase of the solar cycle so that magnetic superstorms may occur in the future.

807

808 **Acknowledgements.** The work of R. H. is funded by the Science & Engineering Research
809 Board (SERB), a statutory body of the Department of Science & Technology (DST),
810 Government of India through Ramanujan Fellowship at NARL. Portions of this research were
811 done at the Jet Propulsion Laboratory, California Institute of Technology, under contract with
812 NASA. G. S. L. thanks the Indian National Science Academy, New Delhi for the support under
813 INSA-Honorary Scientist Scheme. The solar X-ray fluences measured by the GOES/SXI are
814 collected from: <https://www.goes.noaa.gov/>. The SOHO/LASCO CME information are
815 available at: <https://sohowww.nascom.nasa.gov/>. The SDO/AIA CH images are obtained from:
816 <https://sdo.gsfc.nasa.gov/>. The solar wind plasma and IMFs at L1 are obtained from the NASA
817 WIND spacecraft available at: <https://wind.gsfc.nasa.gov/>. The symmetric ring current SYM-
818 H indices are obtained from the World Data Center for Geomagnetism, Kyoto, Japan at:
819 <http://wdc.kugi.kyoto-u.ac.jp/>. The auroral SME and SML indices are taken from the
820 SuperMAG website: <http://supermag.jhuapl.edu/>. The GICs measured in the natural gas
821 pipeline near Mäntsälä, Finland are available from the Space and Earth Observation Centre of
822 the Finnish Meteorological Institute at: <http://space.fmi.fi/>. The NASA Van Allen Probes data
823 are obtained from: <http://vanallenprobes.jhuapl.edu/index.php>. GOES relativistic electron data
824 are collected from: <https://www.goes.noaa.gov/>.

825

826 References

827

- 828 1. Abraham-Schrauner, B. (1972). Determination of magnetohydrodynamic shock
829 normal. *Journal of Geophysical Research*, 77, 736-739.
830 <https://doi.org/10.1029/JA077i004p00736>
- 831 2. Akasofu, S. I., & Chao, J. K. (1980). Interplanetary shock waves and magnetospheric
832 substorms. *Planetary and Space Science*, 28, 381-385. [https://doi.org/10.1016/0032-
833 0633\(80\)90042-2](https://doi.org/10.1016/0032-0633(80)90042-2)
- 834 3. Allen, J., Sauer, H., Frank, L., & Reiff, P. (1989). Effects of the March 1989 solar
835 activity. *Eos Transactions AGU*, 70, 1479-1488. <https://doi.org/10.1029/89EO00409>
- 836 4. Augusto, C. R. A., Navia, C. E., de Oliveira, M. N., Nepomuceno, A. A., Fauth, A. C.,
837 Kopenkin, V., & Sinzi, T. (2019). Relativistic proton levels from region AR 12673
838 (GLE #72) and the heliospheric current sheet as a Sun–Earth magnetic connection.
839 *Publications of the Astronomical Society of the Pacific*, 131:024401.
840 <https://doi.org/10.1088/1538-3873/aaeb7f>
- 841 5. Baker, D. N., Blake, J. B., Callis, L. B., Cummings, J. R., Hovestadt, D., Kanekal, S.,
842 Klecker, B., Mewaldt, R. A., & Zwickl, R. D. (1994). Relativistic electron acceleration
843 and decay time scales in the inner and outer radiation belts: SAMPEX. *Geophysical
844 Research Letters*, 21, 409-412. <https://doi.org/10.1029/93GL03532>

- 845 6. Baker, D. N., Jaynes, A. N., Li, X., Henderson, M. G., Kanekal, S. G., Reeves, G. D.,
846 Spence, H. E., Claudepierre, S. G., Fennell, J. F., Hudson, M. K., Thorne, R. M., Foster,
847 J. C., Erickson, P. J., Malaspina, D. M., Wygant, J. R., Boyd, A., Kletzing, C. A.,
848 Drozdov, A., & Shprits, Y. Y. (2014). Gradual diffusion and punctuated phase space
849 density enhancements of highly relativistic electrons: Van Allen Probes observations.
850 *Geophysical Research Letters*, *41*, 1351-1358. <https://doi.org/10.1002/2013GL058942>
851 7. Balogh, A., Bothmer, V., Crooker, N. U., Forsyth, R. J., Gloeckler, G., Hewish, A.,
852 Hilchenbach, M., Kallenbach, R., Klecker, B., Linker, J. A., Lucek, E., Mann, G.,
853 Marsch, E., Posner, A., Richardson, I. G., Schmidt, J. M., Scholer, M., Wang, Y. M.,
854 Wimmer-Schweingruber, R. F., Aellig, M. R., Bochsler, P., Hefti, S., & Mikić, Z.
855 (1999). The solar origin of corotating interaction regions and their formation in the
856 inner heliosphere. *Space Science Reviews*, *89*, 141-178.
857 <https://doi.org/10.1023/A:1005245306874>
858 8. Berdermann, J., Kriegel, M., Banyś, D., Heymann, F., Hoque, M. M., Wilken, V.,
859 Borries, C., Heßelbarth, A., & Jakowski, N. (2018). Ionospheric response to the X9.3
860 flare on 6 September 2017 and its implication for navigation services over Europe.
861 *Space Weather*, *16*, 1604-1615. <https://doi.org/10.1029/2018SW001933>
862 9. Boteler, D. H. (2003). Geomagnetic hazards to conducting networks. *Natural Hazards*,
863 *28*, 537-561. <https://doi.org/10.1023/A:1022902713136>
864 10. Burlaga, L. F., Ness, N. F., Mariani, F., Bavassano, B., Villante, U., Rosenbauer, H.,
865 Schwenn, R., & Harvey, J. (1978). Magnetic fields and flows between 1 and 0.3 AU
866 during the primary mission of Helios 1. *Journal of Geophysical Research*, *83*, 5167-
867 5174. <https://doi.org/10.1029/JA083iA11p05167>
868 11. Burlaga, L. F., Sittler, E., Mariani, F., & Schwenn, R. (1981). Magnetic loop behind
869 and interplanetary shock: Voyager, Helios and IMP-8 observations. *Journal of*
870 *Geophysical Research*, *6*, 6673-6684. <https://doi.org/10.1029/JA086iA08p06673>
871 12. Chamberlin, P. C., Woods, T. N., Didkovsky, L., Eparvier, F. G., Jones, A. R., Machol,
872 J. L., Mason, J. P., Snow, M., Thiemann, E. M. B., Viereck, R. A., & Woodraska, D.
873 L. (2018). Solar ultraviolet irradiance observations of the solar flares during the intense
874 September 2017 storm period. *Space Weather*, *16*, 1470-1487.
875 <https://doi.org/10.1029/2018SW001866>
876 13. Chertok, I. M., Belov, A. V., & Abunin, A. A. (2018). Solar eruptions, Forbush
877 decreases, and geomagnetic disturbances from outstanding active region 12673. *Space*
878 *Weather*, *16*, 1549-1560. <https://doi.org/10.1029/2018SW001899>
879 14. Clilverd, M. A., Rodger, C. J., Brundell, J. B., Dalzell, M., Martin, I., Mac Manus, D.
880 H., Thomson, N. R., Petersen, T., & Obana, Y. (2018). Long-lasting geomagnetically
881 induced currents and harmonic distortion observed in New Zealand during the 7-8
882 September 2017 disturbed period. *Space Weather*, *16*, 704-717.
883 <https://doi.org/10.1029/2018SW001822>
884 15. Cornwall, J. M. (1965). Cyclotron instabilities and electromagnetic emission in the ultra
885 low frequency and very low frequency ranges. *Journal of Geophysical Research*, *70*,
886 61-69. <https://doi.org/10.1029/JZ070i001p00061>
887 16. Domingo, V., Fleck, B. & Poland, A. I. (1995). The SOHO mission: an overview. *Solar*
888 *Physics*, *162*, 1-37. <https://doi.org/10.1007/BF00733425>
889 17. Dungey, J. W. (1961). Interplanetary magnetic field and the auroral zones. *Physical*
890 *Review Letters*, *6*, 47-48. <https://doi.org/10.1103/PhysRevLett.6.47>
891 18. Echer, E., Gonzalez, W. D., & Tsurutani, B. T. (2008). Interplanetary conditions
892 leading to superintense geomagnetic storms ($Dst \leq -250$ nT) during solar cycle 23.
893 *Geophysical Research Letters*, *35*, L06S03. <https://doi.org/10.1029/2007GL031755>

- 894 19. Echer, E., Tsurutani, B. T., & Guarnieri, F. L. (2009). Solar and interplanetary origins
895 of the November 2004 superstorms. *Advances in Space Research*, 44, 615-620.
896 <https://doi.org/10.1016/j.asr.2009.05.003>
- 897 20. Gjerloev, J. W. (2009). A global ground-based magnetometer initiative. *Eos*
898 *Transactions AGU*, 90, 230-231. <https://doi.org/10.1029/2009EO270002>
- 899 21. Gonzalez, W. D., Tsurutani, B. T., Gonzalez, A. L. C., Smith, E. J., Tang, F., &
900 Akasofu, S.-I. (1989). Solar wind-magnetosphere coupling during intense magnetic
901 storms (1978-1979). *Journal of Geophysical Research*, 94, 8835-8851.
902 <https://doi.org/10.1029/JA094iA07p08835>
- 903 22. Gonzalez, W. D., Joselyn, J. A., Kamide, Y., Kroehl, H. W., Rostoker, G., Tsurutani,
904 B. T., & Vasyliunas, V. M. (1994). What is a geomagnetic storm? *Journal of*
905 *Geophysical Research*, 99, 5771-5792. <https://doi.org/10.1029/93JA02867>
- 906 23. Gopalswamy, N., Lara, A., Yashiro, S., Kaiser, M. L., & Howard, R. A. (2001).
907 Predicting the 1-AU arrival times of coronal mass ejections. *Journal of Geophysical*
908 *Research*, 106, 29207-29217. <https://doi.org/10.1029/2001JA000177>
- 909 24. Hajra, R., & Tsurutani, B. T. (2018a). Interplanetary shocks inducing magnetospheric
910 supersubstorms (SML < -2500 nT): unusual auroral morphologies and energy flow. *The*
911 *Astrophysical Journal*, 858:123. <https://doi.org/10.3847/1538-4357/aabaed>
- 912 25. Hajra, R., & Tsurutani, B. T. (2018b). Magnetospheric “Killer” Relativistic Electron
913 Dropouts (REDs) and Repopulation: A Cyclical Process. In *Extreme Events in*
914 *Geospace: Origins, Predictability, and Consequences*, N. Buzulukova (Editor), Pages
915 373-400, Elsevier. <https://doi.org/10.1016/B978-0-12-812700-1.00014-5>
- 916 26. Hajra, R., Tsurutani, B. T., Echer, E., & Gonzalez, W. D. (2014). Relativistic electron
917 acceleration during high-intensity, long-duration, continuous AE activity (HILDCAA)
918 events: solar cycle phase dependences. *Geophysical Research Letters*, 41, 1876-1881.
919 <https://doi.org/10.1002/2014GL059383>
- 920 27. Hajra, R., Tsurutani, B. T., Echer, E., Gonzalez, W. D., & Gjerloev, J. W. (2016).
921 Supersubstorms (SML < -2500 nT): magnetic storm and solar cycle dependences.
922 *Journal of Geophysical Research: Space Physics*, 121, 7805-7816.
923 <https://doi.org/10.1002/2015JA021835>
- 924 28. Horne, R. B., Lam, M. M., & Green, J. C. (2009). Energetic electron precipitation from
925 the outer radiation belt during geomagnetic storms. *Geophysical Research Letters*, 36,
926 L19104. <https://doi.org/10.1029/2009GL040236>
- 927 29. Hudson, M. K., Baker, D. N., Goldstein, J., Kress, B. T., Paral, J., Toffoletto, F. R., &
928 Wiltberger, M. (2014). Simulated magnetopause losses and Van Allen Probe flux
929 dropouts. *Geophysical Research Letters*, 41, 1113-1118.
930 <https://doi.org/10.1002/2014GL059222>
- 931 30. Illing, R. M. E., & Hundhausen, A. J. (1986). Disruption of a coronal streamer by an
932 eruptive prominence and coronal mass ejection. *Journal of Geophysical Research*, 91,
933 10951-10960. <https://doi.org/10.1029/JA091iA10p10951>
- 934 31. Kanekal, S. G., Baker, D. N., Henderson, M. G., Li, W., Fennell, J. F., Zheng, Y.,
935 Richardson, I. G., Jones, A., Ali, A. F., Elkington, S. R., Jaynes, A., Li, X., Blake, J.
936 B., Reeves, G. D., Spence, H. E., & Kletzing, C. A. (2015). Relativistic electron
937 response to the combined magnetospheric impact of a coronal mass ejection
938 overlapping with a high-speed stream: Van Allen Probes observations. *Journal of*
939 *Geophysical Research: Space Physics*, 120, 7629-7641.
940 <https://doi.org/10.1002/2015JA021395>
- 941 32. Kennel, C. F., & Petschek, H. E. (1966). Limit on stably trapped particle fluxes. *Journal*
942 *of Geophysical Research*, 71, 1-28. <https://doi.org/10.1029/JZ071i001p00001>

- 943 33. Kennel, C. F., Edmiston, J. P., & Hada, T. (1985). A quarter century of collisionless
 944 shock research. In *Collisionless Shocks in the Heliosphere: A Tutorial Review*, edited
 945 by R. G. Stone and B. T. Tsurutani, American Geophysical Union, Washington, D.C.
 946 <https://doi.org/10.1029/GM034p0001>
- 947 34. Kessel, R. L., Fox, N. J., & Weiss, M. (2013). The Radiation Belt Storm Probes (RBSP)
 948 and space weather. *Space Science Reviews*, 179, 531-543.
 949 <https://doi.org/10.1007/s11214-012-9953-6>
- 950 35. Klein, L. W., & Burlaga, L. F. (1982). Interplanetary magnetic clouds at 1 AU. *Journal*
 951 *of Geophysical Research*, 87, 613-624. <https://doi.org/10.1029/JA087iA02p00613>
- 952 36. Kozyra, J. U., Liemohn, M. W., Cattell, C., De Zeeuw, D., Escoubet, C. P., Evans, D.
 953 S., Fang, X., Fok, M.-C., Frey, H. U., Gonzalez, W. D., Hairston, M., Heelis, R., Lu,
 954 G., Manchester IV, W. B., Mende, S., Paxton, L. J., Rastaetter, L., Ridley, A.,
 955 Sandanger, M., Soraas, F., Sotirelis, T., Thomsen, M. W., Tsurutani, B. T., &
 956 Verkhoglyadova, O. (2014). Solar filament impact on 21 January 2005: Geospace
 957 consequences. *Journal of Geophysical Research: Space Physics*, 119, 5401-5448.
 958 <https://doi.org/10.1002/2013JA019748>
- 959 37. Lanzerotti, L. J. (1992). Comment on "Great magnetic storms" by Tsurutani et al.
 960 *Geophysical Research Letters*, 19, 1991-1992. <https://doi.org/10.1029/92GL02238>
- 961 38. Lemen, J. R., Title, A. M., Akin, D. J., et al. (2012). The Atmospheric Imaging
 962 Assembly (AIA) on the Solar Dynamics Observatory (SDO). *Solar Physics*, 275, 17-
 963 40. <https://doi.org/10.1007/s11207-011-9776-8>
- 964 39. Lepri, S. T., & Zurbuchen, T. H. (2010). Direct observational evidence of filament
 965 material within interplanetary coronal mass ejections. *The Astrophysical Journal*, 723,
 966 L22-L27. <https://doi.org/10.1088/2041-8205/723/1/L22>
- 967 40. Li, X., Baker, D. N., Temerin, M. A., Cayton, T. E., Reeves, E. G. D., Christensen, R.
 968 A., Blake, J. B., Looper, M. D., Nakamura, R., & Kanekal, S. G. (1997). Multi-satellite
 969 observations of the outer zone electron variation during the November 3-4, 1993,
 970 magnetic storm. *Journal of Geophysical Research*, 102, 14123-14140.
 971 <https://doi.org/10.1029/97JA01101>
- 972 41. Loomis, E. (1861). On the great auroral exhibition of Aug. 28th to Sept. 4, 1859, and
 973 on auroras generally. *American Journal of Science*, 82, 318-335.
 974 <https://doi.org/10.2475/ajs.s2-32.96.318>
- 975 42. Mauk, B. H., Fox, N. J., Kanekal, S. G., Kessel, R. L., Sibeck, D. G., & Ukhorskiy, A.
 976 (2013). Science objectives and rationale for the Radiation Belt Storm Probes Mission.
 977 *Space Science Reviews*, 179, 3-27. <https://doi.org/10.1007/s11214-012-9908-y>
- 978 43. Meng, X., Tsurutani, B. T., & Mannucci, A. J. (2019). The solar and interplanetary
 979 causes of superstorms (minimum Dst ≤ -250 nT) during the space age. *Journal of*
 980 *Geophysical Research: Space Physics*, 124. <https://doi.org/10.1029/2018JA026425>
- 981 44. Meredith, N. P., Cain, M., Horne, R. B., Thorne, R. M., Summers, D., & Anderson, R.
 982 R. (2003). Evidence for chorus-driven electron acceleration to relativistic energies from
 983 a survey of geomagnetically disturbed periods. *Journal of Geophysical Research*, 108,
 984 1248. <https://doi.org/10.1029/2002JA009764>
- 985 45. Meurant, M., Gérard, J.-C., Blockx, C., Coumans, V., Hubert, B., Connors, M., Lyons,
 986 L. R., & Donovan, E. (2005). Comparison of intense nightside shock-induced
 987 precipitation and substorm activity. *Journal of Geophysical Research*, 110, A07228.
 988 <https://doi.org/10.1029/2004JA010916>
- 989 46. Michalek, G., Gopalswamy, N., Lara, A., & Manoharan, P. K. (2004). Arrival time of
 990 halo coronal mass ejections in the vicinity of the Earth. *Astronomy & Astrophysics*, 423,
 991 729-736. <https://doi.org/10.1051/0004-6361:20047184>

- 992 47. Ness, N. F., & Wilcox, J. M. (1964). Solar origin of the interplanetary magnetic field.
993 *Physical Review Letters*, 13, 461-464. <https://doi.org/10.1103/PhysRevLett.13.461>
- 994 48. Onsager, T., Grubb, R., Kunches, J., Matheson, L., Speich, D., Zwickl, R. W., & Sauer,
995 H. (1996). Operational uses of the GOES energetic particle detectors. In *Proceedings*
996 *SPIE 2812, GOES-8 and Beyond 281*. <https://doi.org/10.1117/12.254075>
- 997 49. Pirjola, R. (2000). Geomagnetically induced currents during magnetic storms. *IEEE*
998 *Transactions on Plasma Science*, 28, 1867-1873. <https://doi.org/10.1109/27.902215>
- 999 50. Pizzo, V. J. (1985). Interplanetary shocks on the large scale: a retrospective on the last
1000 decade's theoretical efforts. In *Collisionless Shocks in the Heliosphere: Reviews of*
1001 *Current Research*, Geophysical Monograph Series, 35, edited by B. T. Tsurutani and
1002 R. G. Stone, 51-68, AGU, Washington, D.C. <https://doi.org/10.1029/GM035p0051>
- 1003 51. Pulkkinen, A., Viljanen, A., Pajunpää, K., & Pirjola, R. (2001). Recordings and
1004 occurrence of geomagnetically induced currents in the Finnish natural gas pipeline
1005 network. *Journal of Applied Geophysics*, 48, 219-231. [https://doi.org/10.1016/S0926-](https://doi.org/10.1016/S0926-9851(01)00108-2)
1006 [9851\(01\)00108-2](https://doi.org/10.1016/S0926-9851(01)00108-2)
- 1007 52. Redmon, R. J., Seaton, D. B., Steenburgh, R., He, J., & Rodriguez, J. V. (2018).
1008 September 2017's geoeffective space weather and impacts to Caribbean radio
1009 communications during hurricane response. *Space Weather*, 16, 1190-1201.
1010 <https://doi.org/10.1029/2018SW001897>
- 1011 53. Remya, B., Tsurutani, B. T., Reddy, R. V., Lakhina, G. S., & Hajra, R. (2015).
1012 Electromagnetic cyclotron waves in the dayside subsolar outer magnetosphere
1013 generated by enhanced solar wind pressure: EMIC wave coherency. *Journal of*
1014 *Geophysical Research: Space Physics*, 120, 7536-7551.
1015 <https://doi.org/10.1002/2015JA021327>
- 1016 54. Schillings, A., Nilsson, H., Slapak, R., Wintoft, P., Yamauchi, M., Wik, M., Dandouras,
1017 I., & Carr, C. M. (2018). O⁺ escape during the extreme space weather event of 4-10
1018 September 2017. *Space Weather*, 16, 1363-1376.
1019 <https://doi.org/10.1029/2018SW001881>
- 1020 55. Seaton, D. B., & Darnel, J. M. (2018). Observations of an eruptive solar flare in the
1021 extended EUV solar corona. *The Astrophysical Journal Letters*, 852, L9.
1022 <https://doi.org/10.3847/2041-8213/aaa28e>
- 1023 56. Sheeley, N. R., & Harvey, J. W. (1981). Coronal holes, solar wind streams, and
1024 geomagnetic disturbances during 1978 and 1979. *Solar Physics*, 70, 237-249.
1025 <https://doi.org/10.1007/BF00151331>
- 1026 57. Shen, C., Xu, M., Wang, Y., Chi, Y., & Luo, B. (2018). Why the shock-ICME complex
1027 structure is important: learning from the early 2017 September CMEs. *The*
1028 *Astrophysical Journal*, 861:28. <https://doi.org/10.3847/1538-4357/aac204>
- 1029 58. Smith, E. J. (1985). Interplanetary shock phenomena beyond 1 AU. In *Collisionless*
1030 *Shocks in the Heliosphere: Reviews of Current Research*, Geophysical Monograph
1031 Series, vol. 35, edited by B. T. Tsurutani and R. G. Stone, 69 pp., AGU, Washington,
1032 D. C. <https://doi.org/10.1029/GM035p0069>
- 1033 59. Smith, E. J., & Wolfe, J. H. (1976). Observations of interaction regions and corotating
1034 shocks between one and five AU: pioneers 10 and 11. *Geophysical Research Letters*,
1035 3, 137-140. <https://doi.org/10.1029/GL003i003p00137>
- 1036 60. Smith, E. J., Tsurutani, B. T., & Rosenberg, R. L. (1978). Observations of the
1037 interplanetary sector structure up to heliographic latitudes of 16°: Pioneer 11. *Journal*
1038 *of Geophysical Research*, 83, 717-724. <https://doi.org/10.1029/JA083iA02p00717>
- 1039 61. Sugiura, M. (1964). Hourly Values of Equatorial Dst for the IGY, Annual International
1040 Geophysical Year, vol. 35, p. 9, Pergamon, New York

- 1041 62. Summers, D., Ni, B., & Meredith, N. P. (2007). Timescale for radiation belt electron
 1042 acceleration and loss due to resonant wave-particle interactions: 2. Evaluation for VLF
 1043 chorus, ELF hiss, and electromagnetic ion cyclotron waves. *Journal of Geophysical*
 1044 *Research*, *112*, A04207. <https://doi.org/10.1029/2006JA011993>
- 1045 63. Tang, F., Tsurutani, B. T., Gonzalez, W. D., Akasofu, S. I., & Smith, E. J. (1989). Solar
 1046 sources of interplanetary southward Bz events responsible for major magnetic storms
 1047 (1978-1979). *Journal of Geophysical Research*, *94*, 3535-3541.
 1048 <https://doi.org/10.1029/JA094iA04p03535>
- 1049 64. Thorne, R. M., & Kennel, C. F. (1971). Relativistic electron precipitation during
 1050 magnetic storm main phase. *Journal of Geophysical Research*, *76*, 4446-4453.
 1051 <https://doi.org/10.1029/JA076i019p04446>
- 1052 65. Tsurutani, B. T., & Gonzalez, W. D. (1987). The cause of high-intensity long-duration
 1053 continuous AE activity (HILDCAAs): Interplanetary Alfvén wave trains. *Planetary*
 1054 *and Space Science*, *35*, 405-412. [https://doi.org/10.1016/0032-0633\(87\)90097-3](https://doi.org/10.1016/0032-0633(87)90097-3)
- 1055 66. Tsurutani, B. T., & Lin, R. P. (1985). Acceleration of > 47 keV ions and > 2 keV
 1056 electrons by interplanetary shocks at 1 AU. *Journal of Geophysical Research*, *90*, 1-11.
 1057 <https://doi.org/10.1029/JA090iA01p00001>
- 1058 67. Tsurutani, B. T., Gonzalez, W. D., Tang, F., Akasofu, S. I., & Smith, E. J. (1988).
 1059 Origin of interplanetary southward magnetic fields responsible for major magnetic
 1060 storms near solar maximum (1978-1979). *Journal of Geophysical Research*, *93*, 8519-
 1061 8531. <https://doi.org/10.1029/JA093iA08p08519>
- 1062 68. Tsurutani, B. T., Gonzalez, W. D., Tang, F., & Lee, Y. T. (1992). Great magnetic
 1063 storms. *Geophysical Research Letters*, *19*, 73-76. <https://doi.org/10.1029/91GL02783>
- 1064 69. Tsurutani, B. T., Gonzalez, W. D., Gonzalez, A. L. C., Tang, F., Arballo, J. K., &
 1065 Okada, M. (1995). Interplanetary origin of geomagnetic activity in the declining phase
 1066 of the solar cycle. *Journal of Geophysical Research*, *110*, 21717-21733.
 1067 <https://doi.org/10.1029/95JA01476>
- 1068 70. Tsurutani, B. T., Gonzalez, W. D., Gonzalez, A. L. C., Guarnieri, F. L., Gopalswamy,
 1069 N., Grande, M., Kamide, Y., Kasahara, Y., Lu, G., McPherron, R. L., Soraas, F., &
 1070 Vasyliunas, V. (2006). Corotating solar wind streams and recurrent geomagnetic
 1071 activity: a review. *Journal of Geophysical Research*, *111*, A07S01.
 1072 <https://doi.org/10.1029/2005JA011273>
- 1073 71. Tsurutani, B. T., Echer, E., & Gonzalez, W. D. (2011). The solar and interplanetary
 1074 causes of the recent minimum in geomagnetic activity (MGA23): a combination of
 1075 midlatitude small coronal holes, low IMF Bz variances, low solar wind speeds and low
 1076 solar magnetic fields. *Annales Geophysicae*, *29*, 839-849.
 1077 <https://doi.org/10.5194/angeo-29-839-2011>
- 1078 72. Tsurutani, B. T., Hajra, R., Echer, E., & Gjerloev, J. W. (2015). Extremely intense
 1079 (SML \leq -2500 nT) substorms: isolated events that are externally triggered? *Annales*
 1080 *Geophysicae*, *33*, 519-524. <https://doi.org/10.5194/angeo-33-519-2015>
- 1081 73. Tsurutani, B. T., et al. (2016). Heliospheric plasma sheet (HPS) impingement onto the
 1082 magnetosphere as a cause of relativistic electron dropouts (REDs) via coherent EMIC
 1083 wave scattering with possible consequences for climate change mechanisms. *Journal*
 1084 *of Geophysical Research: Space Physics*, *121*, 10130-10156.
 1085 <https://doi.org/10.1002/2016JA022499>
- 1086 74. Tsurutani, B. T., Park, S. A., Falkowski, B. J., Lakhina, G. S., Pickett, J. S., Bortnik, J.,
 1087 Hospodarsky, G., Santolik, O., Parrot, M., Henri, P., & Hajra, R. (2018). Plasmaspheric
 1088 hiss: coherent and intense. *Journal of Geophysical Research: Space Physics*, *123*,
 1089 10009-10029. <https://doi.org/10.1029/2018JA025975>

- 1090 75. Van Allen, J. A., & Frank, L. A. (1959). Radiation measurements to 658,300 km with
1091 Pioneer IV. *Nature*, *184*, 219-224. <https://doi.org/10.1038/184219a0>
- 1092 76. Viljanen, A., Nevanlinna, H., Pajunpää, K., & Pulkkinen, A. (2001). Time derivative
1093 of the horizontal geomagnetic field as an activity indicator. *Annales Geophysicae*, *19*,
1094 1107-1118. <https://doi.org/10.5194/angeo-19-1107-2001>
- 1095 77. Viljanen, A., Pulkkinen, A., Pirjola, R., Pajunpää, K., Posio, P., & Koistinen, A. (2006).
1096 Recordings of geomagnetically induced currents and a nowcasting service of the
1097 Finnish natural gas pipeline system. *Space Weather*, *4*, S10004.
1098 <https://doi.org/10.1029/2006SW000234>
- 1099 78. Wanliss, J. A., & Showalter, K. M. (2006). High-resolution global storm index: Dst
1100 versus SYM-H. *Journal of Geophysical Research*, *111*, A02202.
1101 <https://doi.org/10.1029/2005JA011034>
- 1102 79. West Jr., H. I., Buck, R. M., & Walton, J. R. (1972). Shadowing of electron azimuthal-
1103 drift motions near the noon magnetopause. *Nature Physical Science*, *240*, 6-7.
1104 <https://doi.org/10.1038/physci240006a0>
- 1105 80. Winterhalter, D., Smith, E. J., Burton, M. E., Murphy, N., & McComas, D. J. (1994).
1106 The heliospheric plasma sheet. *Journal of Geophysical Research*, *99*, 6667-6680.
1107 <https://doi.org/10.1029/93JA03481>
- 1108 81. Yan, X. L., Wang, J. C., Pan, G. M., Kong, D. F., Xue, Z. K., Yang, L. H., Li, Q. L., &
1109 Feng, X. S. (2018). Successive X-class flares and coronal mass ejections driven by
1110 shearing motion and sunspot rotation in active region NOAA 12673. *The Astrophysical*
1111 *Journal*, *856*:79. <https://doi.org/10.3847/1538-4357/aab153>
- 1112 82. Zhang, J., Richardson, I. G., Webb, D. F., Gopalswamy, N., Huttunen, E., Kasper, J.
1113 C., Nitta, N. V., Poomvises, W., Thompson, B. J., Wu, C. C., Yashiro, S., Zhukov, A.
1114 N. (2007). Solar and interplanetary sources of major geomagnetic storms ($Dst \leq -100$
1115 nT) during 1996-2005. *Journal of Geophysical Research*, *112*, A10102.
1116 <https://doi.org/10.1029/2007JA012321>
- 1117 83. Zhou, X., & Tsurutani, B. T. (2001). Interplanetary shock triggering of nightside
1118 geomagnetic activity: substorms, pseudobreakups, and quiescent events. *Journal of*
1119 *Geophysical Research*, *106*, 18957-18967. <https://doi.org/10.1029/2000JA003028>
- 1120 84. Zhou, G., Wang, J., & Cao, Z. (2003). Correlation between halo coronal mass ejections
1121 and solar surface activity. *Astronomy & Astrophysics*, *397*, 1057-1067.
1122 <https://doi.org/10.1051/0004-6361:20021463>
- 1123 85. Zou, P., Jiang, C., Feng, X., Zuo, P., Wang, Y., & Wei, F. (2019). A two-step magnetic
1124 reconnection in a confined X-class flare in solar active region 12673. *The Astrophysical*
1125 *Journal*, *870*:97. <https://doi.org/10.3847/1538-4357/aaf3b7>
- 1126
1127
1128
1129
1130
1131
1132
1133
1134
1135
1136
1137
1138
1139

Tables

1140
1141
1142
1143

Table 1. X-class solar flares recorded during September 2017

Flare no.	Date	Start time (UT)	Peak time (UT)	End time (UT)	Class	Location
XFlare1	06/09	08:57	09:10	09:17	X2.2	S08W33
XFlare2	06/09	11:53	12:02	12:10	X9.3	S08W33
XFlare3	07/09	14:20	14:36	14:55	X1.3	S11W49
XFlare4	10/09	15:35	16:06	16:31	X8.2	S14W74

1144
1145
1146

Table 2. Propagation prediction of halo CMEs to the Earth

CME no.	CME time (UT)	V_{CME} (km s ⁻¹)	Predicted time at 1 AU (UT)			Observed FS time at 1 AU (UT)	Error (h)		
			Mod1	Mod2	Mod3		Mod1	Mod2	Mod3
hCME1	04/09	1418	06/09	06/09	06/09	06/09	11.4	13.3	3.2
	20:36		11:46	09:50	19:55	23:02			
hCME2	06/09	1571	07/09	07/09	08/09	07/09	-0.4	0.6	-6.3
	12:24		22:48	21:36	04:34	22:19			
hCME3	10/09	3163	11/09	11/09	11/09	12/09	36.3	36.1	35.4
	16:00		06:58	07:12	07:55	19:12			
hCME4	17/09	1385	19/09	19/09	19/09	No significant ICME signature			
	12:00		04:19	02:10	13:12				

1147

Table 3. Characteristics of the interplanetary discontinuities at WIND spacecraft

Time (UT)	Type	Jump in interplanetary parameters					θ_{Bn} (°)	MMN	Impacts
		V_{sw} (km s ⁻¹)	N_{sw} (cm ⁻³)	P_{sw} (nPa)	T_{sw} (10 ⁴ K)	B_0 (nT)			
06/09 23:02	FS1	410-575	2-14	2-13	2-40	2-6	89.8	5.80	SI+ ~+56 nT
07/09 22:19	FS2	475-680	3-4	2-9	2-80	10-22	47.9	6.73	SI+ ~+20 nT, SSS (SME 4464 nT, SML -3712 nT)
12/09 19:12	FS3	460-620	5-17	2-16	12-56	4-8	19.4	3.97	SI+ ~+27 nT, substorm (SME 1366 nT, SML -1071 nT)
14/09 00:00	FS4	350-370	5-12	1-4	3-8	2-5	8.5	4.30	SI+ ~+14 nT
14/09 10:05	FS5	345-419	10-33	2-9	7-9	2-4	84.0	1.73	SI+ ~+28 nT
14/09 14:10	HCS1	436-474	11-40	4-20	11-37	4-10			Substorm (SME 1171 nT, SML -766 nT)
14/09 18:29	RW1	473-630	11-4	15-2	36-19	10-5	71.2	0.84	SI- ~-23 nT, substorm recovery
24/09 21:22	HCS2	330-370	5-36	1-7	2-5	4-9			No substorm
26/09 22:48	FS6	310-333	13-21	2-6	1-5	4-7	33.5	2.72	SI+ ~+14 nT
27/09 05:17	HCS3	350-530	18-54	4-14	4-40	9-16			Substorm (SME 883 nT, SME -614 nT) (07:39)
28/09 08:38	RW2	651-692	7-4	7-2	37-25	7-3	86.7	0.71	SI- ~-14 nT, substorm recovery

1148
1149
1150
1151
1152
1153
1154
1155
1156
1157
1158
1159
1160
1161

1162 **Table 4.** Interplanetary sheaths and MCs

1163

Type	Start time (UT)	End time (UT)	Peak IMF Bz (nT)	Impacts
Sheath1	06/09 23:02	07/09 22:19	-11	Substorm (SME 1417 nT, SML -1097 nT)
Sheath2	07/09 22:19	08/09 11:02	-31	Intense storm (SYM-H -146 nT), SSS (SME 4464 nT, SML -3712 nT)
MC	08/09 11:02	11/09 00:43	-17	Intense storm (SYM-H -115 nT), SSS (SME 4330 nT, SML -2642 nT)
Sheath3	12/09 19:12	13/09 03:22	-12	Moderate storm (SYM-H -65 nT), substorm (SME 1366 nT, SML -1071 nT), substorm (SME 1856 nT, SML -1541 nT)
Sheath4	14/09 00:00	14/09 10:05	-4	Substorm (SME 389 nT, SML -306 nT)

1164

1165 **Table 5.** Interplanetary HSSs and CIRs

1166

Type	Start time (UT)	End time (UT)	V _{sw} (km s ⁻¹)	Impacts
HSS1	01/09 04:09	02/09 23:18	687	Intense auroral (SME ~1588 nT, SML ~-1439 nT) activity
HSS2	14/09 18:43	18/09 22:29	743	Intense auroral (SME ~1749 nT, SML ~-1423 nT) activity
HSS3	27/09 15:41	29/09 22:16	721	Intense auroral (SME ~2044 nT, SML ~-949 nT) activity
CIR1	14/09 10:05	14/09 18:29	333-743	No storm/substorm
CIR2	26/09 22:48	28/09 08:38	315-721	Moderate storm (SYM-H -74 nT), substorm (SME 2683 nT, SML -1813 nT)

1167

1168 **Table 6.** SSSs and GICs

1169

SSS no.	SSS interval		SSS strength		GIC impact	
	Start (UT)	End (UT)	SML peak	Time (UT)	GIC peak (A)	Time (LT)
SSS1	07/09	08/09	-3712	08/09	28.2	08/09
	22:19	02:51		00:24		03:31
SSS2	08/09	08/09	-2642	08/09	30.4	08/09
	11:34	15:42		13:08		20:55

1170

1171

1172

1173

1174

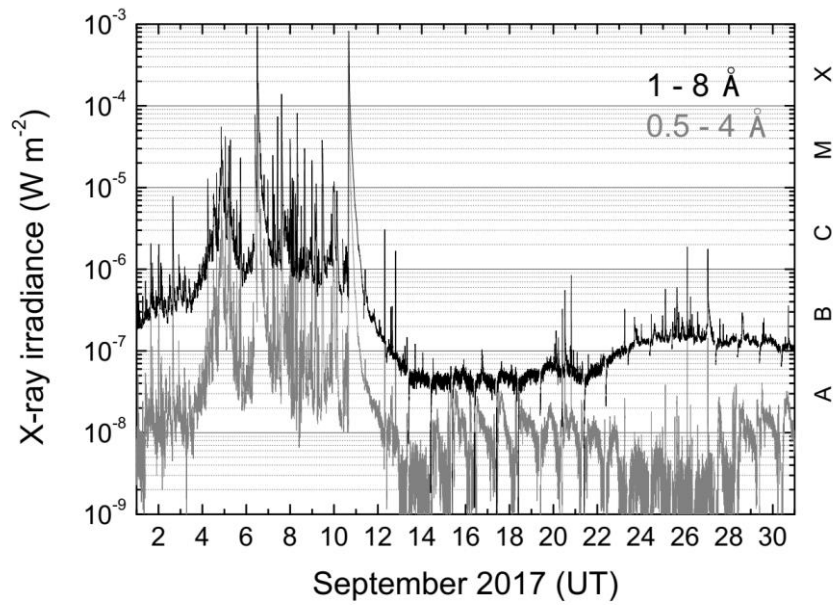
1175

1176

1177

1178

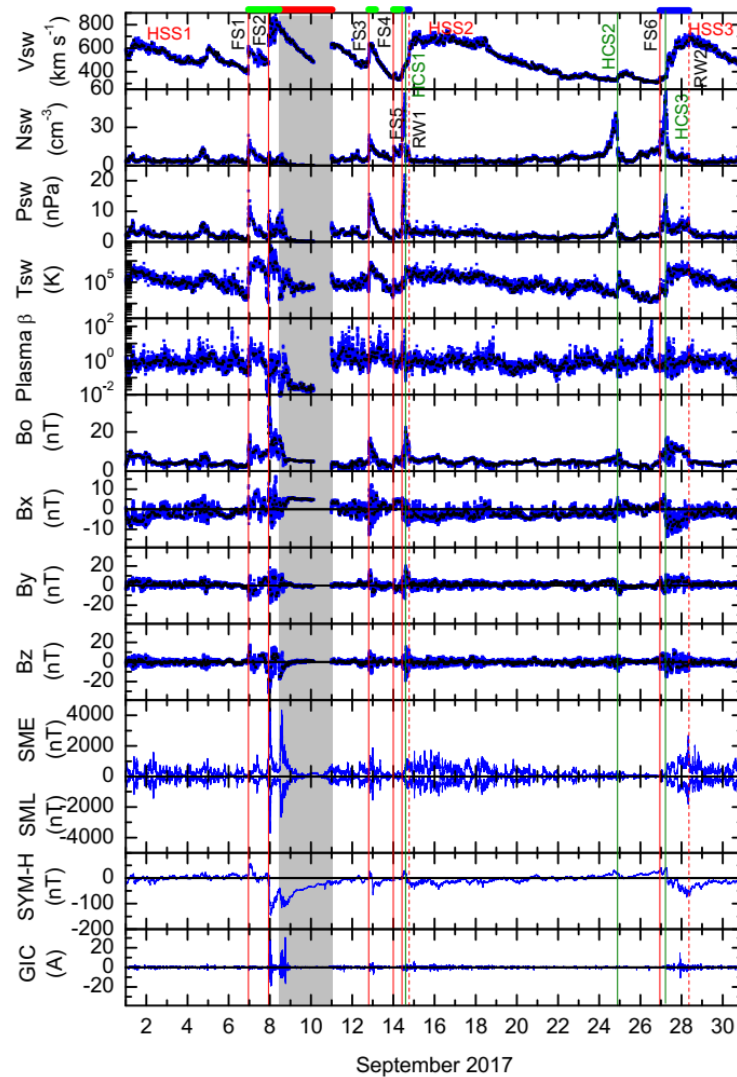
Figures and Captions

1179
1180

1181
1182 **Figure 1.** The GOES x-ray irradiance during September 2017. Classes of x-ray flares are
1183 marked on the right.

1184
1185
1186
1187
1188
1189
1190
1191
1192
1193
1194
1195
1196
1197
1198
1199
1200
1201
1202
1203
1204
1205
1206
1207
1208
1209
1210
1211

1212



1213

1214

1215 **Figure 2.** Solar wind/interplanetary and geomagnetic variations during September 2017. From

1216 top to bottom, the panels show the solar wind plasma speed (V_{sw}), density (N_{sw}), ram pressure

1217 (P_{sw}), plasma temperature (T_{sw}), plasma beta (β), interplanetary magnetic field (IMF)

1218 amplitude B_0 , and B_x , B_y , B_z components in geocentric solar magnetospheric (GSM)

1219 coordinate system, auroral electrojet SME and SML indices, symmetric ring current SYM-H

1220 index, and geomagnetically induced current (GIC), respectively. The blue and black data points

1221 correspond to 1 min and 1 h resolution, respectively. Vertical red solid, red dashed and green

1222 solid lines indicate FSS, RWs and HCSs, respectively. On the top, green, red and blue

1223 horizontal bars indicate the interplanetary sheath, MC and CIR intervals, respectively.

1224

1225

1226

1227

1228

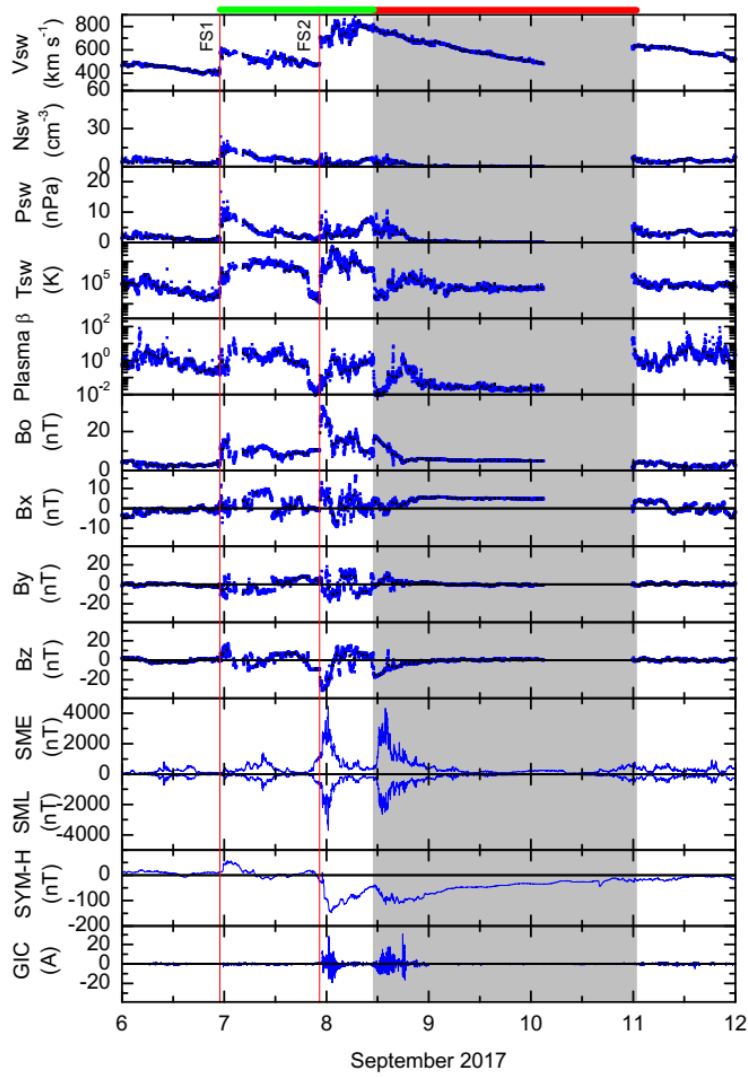
1229

1230

1231

1232

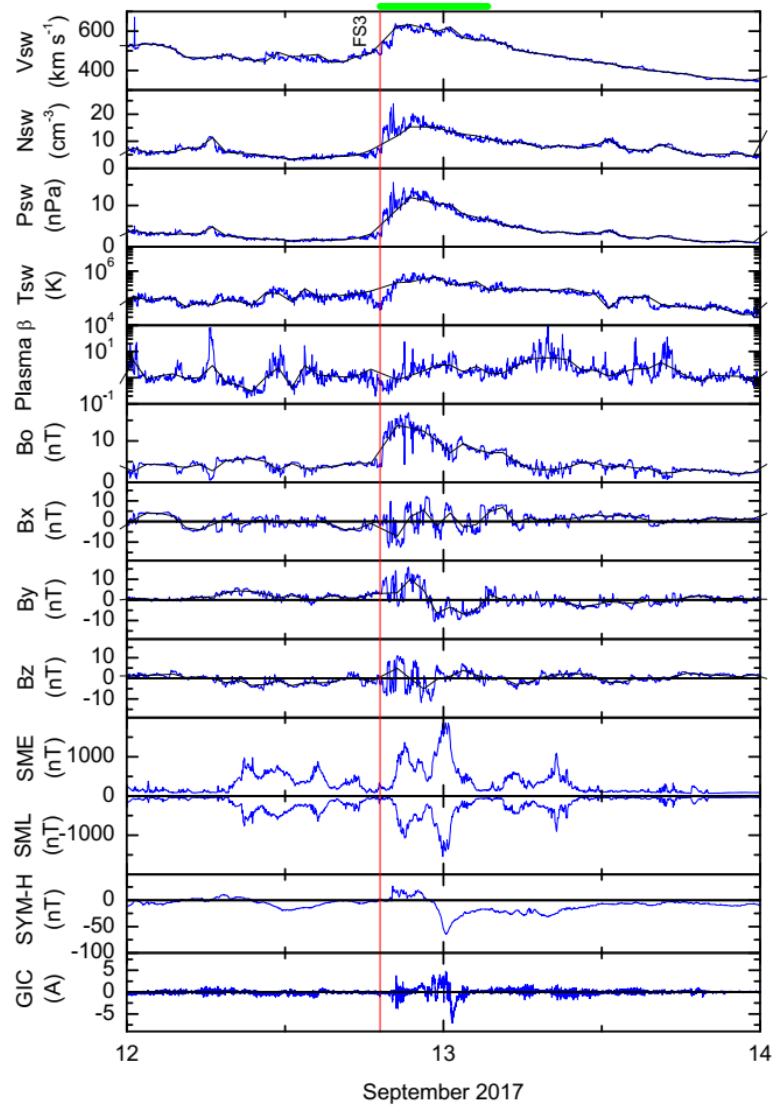
1233



1234
 1235
 1236
 1237
 1238
 1239
 1240
 1241
 1242
 1243
 1244
 1245
 1246
 1247
 1248
 1249
 1250
 1251
 1252
 1253
 1254

Figure 3. Solar wind/interplanetary and geomagnetic variations during 6 – 11 September 2017. The panels are in same format as in Figure 2.

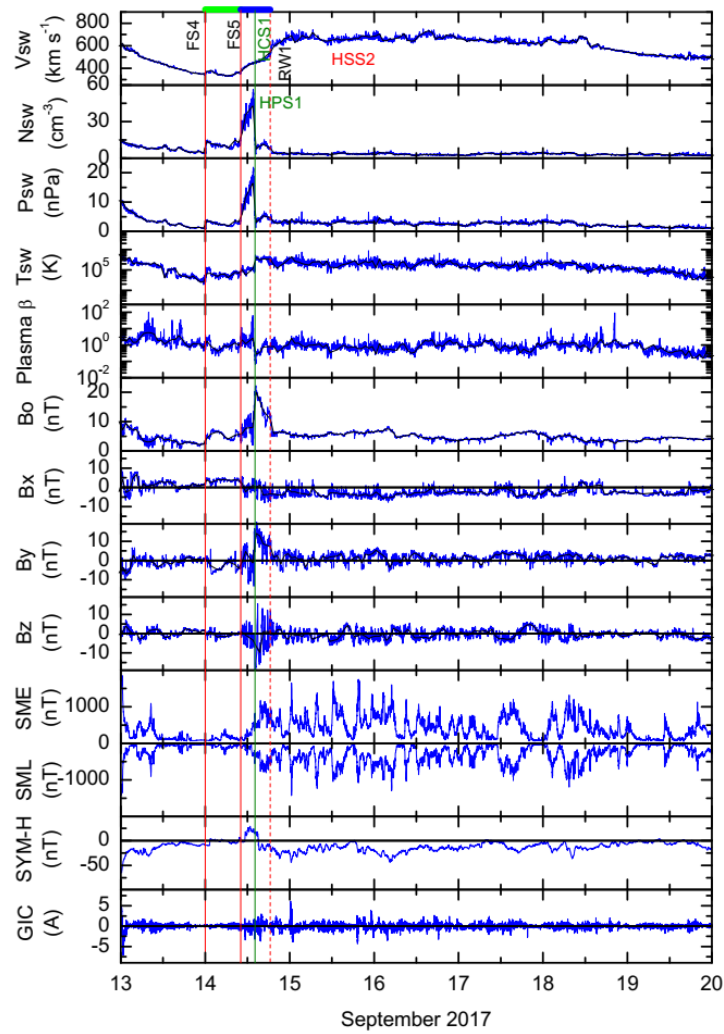
1255



1256
 1257
 1258
 1259
 1260
 1261
 1262
 1263
 1264
 1265
 1266
 1267
 1268
 1269
 1270
 1271
 1272
 1273
 1274
 1275

Figure 4. Solar wind/interplanetary and geomagnetic variations during 12 – 13 September 2017. The panels are in same format as in Figure 2.

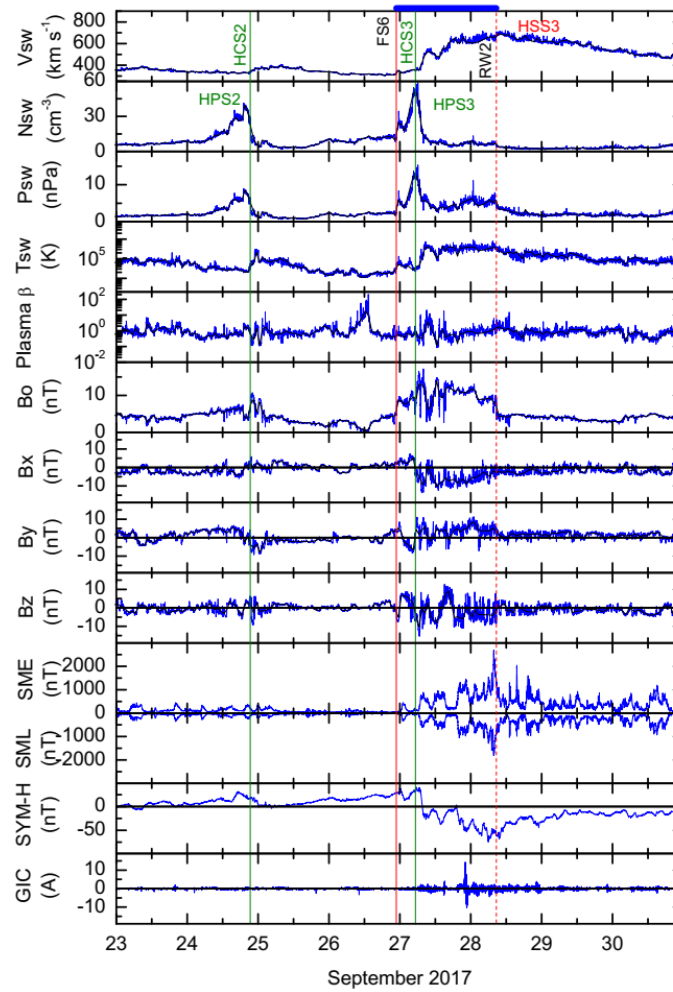
1276



1277
 1278
 1279
 1280
 1281
 1282
 1283
 1284
 1285
 1286
 1287
 1288
 1289
 1290
 1291
 1292
 1293
 1294
 1295
 1296
 1297
 1298

Figure 5. Solar wind/interplanetary and geomagnetic variations during 13 – 19 September 2017. The panels are in same format as in Figure 2.

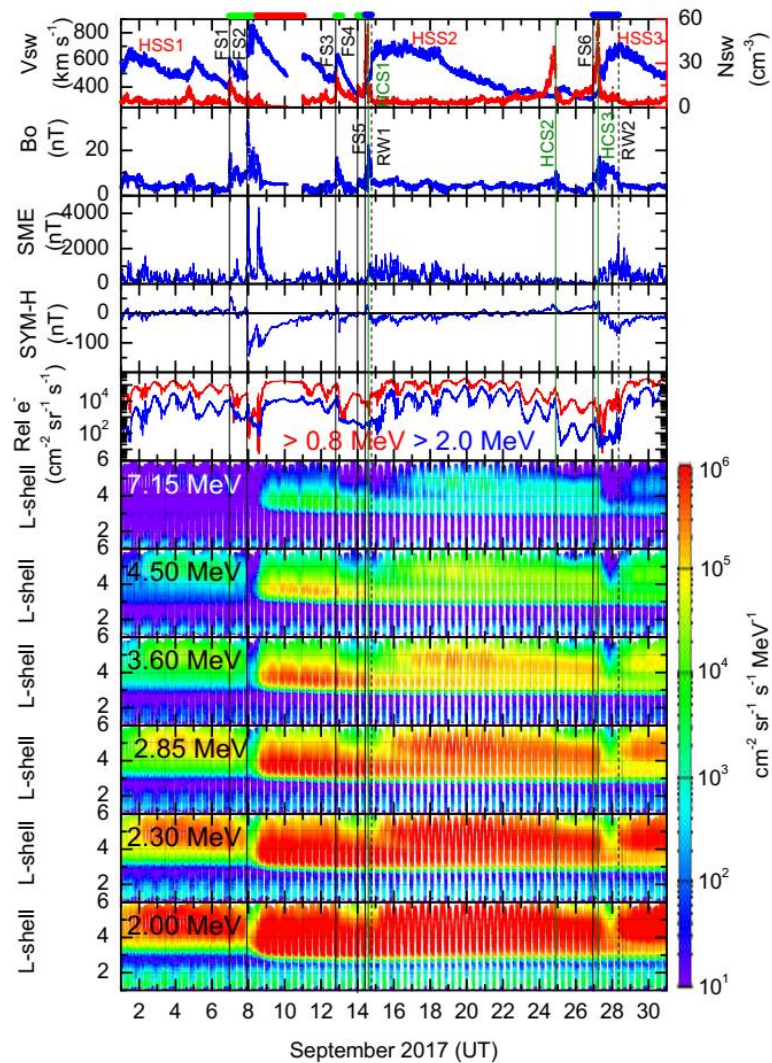
1299



1300
 1301
 1302
 1303
 1304
 1305
 1306
 1307
 1308
 1309
 1310
 1311
 1312
 1313
 1314
 1315
 1316
 1317
 1318
 1319
 1320
 1321
 1322

Figure 6. Solar wind/interplanetary and geomagnetic variations during 23 – 30 September 2017. The panels are in same format as in Figure 2.

1323



1324

1325

Figure 7. Response of the outer zone radiation belt relativistic electron fluxes to the complex

and multiple space weather events. In the top four panels interplanetary and geomagnetic data

from Figure 2 are repeated to give reference to interplanetary and geomagnetic events. The

fifth panel from the top displays relativistic > 0.8 MeV and > 2.0 MeV electron fluxes at

geosynchronous GOES 15 orbit. The bottom six panels show the L-shell variations of 7.15

MeV, 4.50 MeV, 3.60 MeV, 2.85 MeV, 2.30 MeV and 2.00 MeV electron fluxes measured by

the REPT instrument on VAPs, respectively. Flux values are shown in the colour scale on the

right. Vertical black solid, black dashed and green solid lines indicate FSs, RWs and HCSs,

respectively. On the top, green, red and blue horizontal bars indicate the interplanetary sheath,

MC and CIR intervals, respectively.

1334